Holocene temperature and water stress in the Peruvian Andes: insights from lake carbonate clumped and triple oxygen isotopes

Authors: Sarah A. Katz[1*], Naomi E. Levin[1], Mark B. Abbott[2], Donald T. Rodbell[3], Benjamin H. Passey[1], Nicole M. DeLuca[4], Darren J. Larsen[5], Arielle Woods[2]

[1]Department of Earth and Environmental Sciences, 1100 North University Ave, University of Michigan, Ann Arbor, MI, 48109, USA
[2]Department of Geology and Environmental Science, 4107 O'Hara Street, University of Pittsburgh, Pittsburgh, PA, 15260, USA
[3]Geosciences Department, 807 Union Street, Union College, Schenectady, NY, 12308, USA
[4]Department of Earth and Planetary Sciences, Johns Hopkins University, 3400 North Charles Street, Baltimore, MD, 21218, USA
[5]Geology Department, 1600 Campus Road, Occidental College, Los Angeles, CA, 90042, USA

* Corresponding author: Sarah Katz (skatzees@umich.edu)

Key points:

1. Lake carbonate $\Delta'^{17}O$ and Δ_{47} constrain lake temperature and water balance histories in ways that $\delta^{18}O$ records alone cannot resolve.
2. Carbonate $\Delta'^{17}O$ records from 3 Andean lakes indicate that lake hydrology and regional water balance track insolation across the Holocene.
3. Low $\Delta'^{17}O$ for reconstructed lake water indicates that greater evaporative conditions correspond to weakened early and mid-Holocene SASM.

Abstract:

Global climate during the Holocene was relatively stable compared to the late Pleistocene. However, evidence from lacustrine records in South America suggests that tropical latitudes experienced significant water balance variability during the Holocene, rather than quiescence. For example, a tight coupling between insolation and carbonate $\delta^{18}O$ records from central Andean lakes (e.g., Lakes Junín, Pumacocha) suggest water balance is tied directly to South American summer monsoon (SASM) strength. However, lake carbonate $\delta^{18}O$ records also incorporate information about temperature and evaporation. To overcome this ambiguity, clumped and triple oxygen isotope records can provide independent constraints on temperature and evaporation. Here, we use clumped and triple oxygen isotopes to develop Holocene temperature and evaporation records from three central Andean lakes, Lakes Junín, Pumacocha, and Mehcocha, to build a more complete picture of regional water balance (*P–E*). We find that Holocene water temperatures at all three lakes were stable and slightly warmer than during the latest Pleistocene. These results are consistent with global data assimilations and records from the foothills and Amazon basin. In contrast, evaporation was highly variable and tracks SASM intensity. The hydrologic response of each lake to SASM depends greatly on the physical characteristics of the lake basin, but they all record peak evaporation in the early to mid-Holocene (11,700 to 4,200 years BP) when regional insolation was relatively low and the SASM was weak. These results corroborate other central Andean records and suggest synchronous, widespread water stress tracks insolation-paced variability in SASM strength.

Keywords: Holocene, Andes, temperature, water balance, lacustrine carbonate, lake hydrology, triple oxygen isotopes, clumped isotopes

1. Introduction:

During the Holocene, the central Andes witnessed ecological turnover (e.g., Hansen et al., 1994; Rozas-Davila et al., 2023; Schiferl et al., 2023), net loss of mountain glaciers (e.g., Rodbell et al., 2008, 2009; Stansell et al., 2013, 2017; Palacios et al., 2020), and expansion of pre-Columbian societies (e.g., Rademaker et al., 2014; de Souza et al., 2019; Riris and Arroyo-Kalin, 2019). Water plays a crucial role in these dynamics, such that hydrologic records from the Holocene (11,700 years before present (i.e., "years BP") to present day) provide insights into the rise of modern environments and the sensitivity of these regions to global climate change (Thompson et al., 1995; Cruz et al., 2005; Rodbell et al., 2022). Many studies have documented the relationship between global climate and the central Andean water cycle during the Holocene (e.g., Seltzer et al., 2000; Woods et al., 2020), as global insolation and high latitude feedbacks control the position of the intertropical convergence zone and the convective strength of the South American summer monsoon (SASM) (e.g., Vuille et al., 2012; McGee et al., 2014; Liu and Battisti, 2015; Woods et al., 2020). However, few studies document how local water balance ($P–E$) has changed in response to SASM variability, such that we lack information about how local $P–E$ relates to global climate change (e.g., Ward et al., 2019; Woods et al., 2020).

The SASM is the primary atmospheric system in the tropical and subtropical latitudes of South America (10 °N–30 °S) and conveys moist air masses from the Atlantic westward over the Amazon basin and central Andes (Lenters and Cook, 1999; Vera et al., 2006; Garreaud et al., 2009; Marengo et al., 2012). Convective intensity (i.e., SASM "strength") and geographic position are controlled by meridional temperature gradients in the Atlantic, such that precession-paced changes in insolation drive rainfall trends in the core monsoon region on millennial–orbital timescales (Figure 1a) (Cruz et al., 2005; Liu and Battisti, 2015). SASM strength is greatest when southern hemisphere summer (Dec–Feb) insolation is highest (i.e., the late Holocene) and weakest when local summer insolation is low (i.e., the early Holocene) (Figure 1a) (Laskar et al., 2004; McGee et al., 2014).

Oxygen isotopes ($\delta^{18}O$) of precipitation are a common tool used to explore water cycle processes, including SASM dynamics, because isotopes integrate information about atmospheric and terrestrial conditions (Craig, 1961; Dansgaard, 1964; Rozanski et al., 1993). For example, in the monsoon region, the $\delta^{18}O$ value of rainfall can be explained by Rayleigh distillation, whereby precipitation $\delta^{18}O$ values reflect the degree of rainout at upwind sites. In South America, this leads to a predictable, continental-scale pattern of decreasing precipitation $\delta^{18}O$ values from east to west, corresponding to progressive loss of the heavier isotopes. Under weak SASM conditions during the early Holocene (e.g., 11,700 to 8,200 years BP), the continental $\delta^{18}O$ gradient is weaker compared to a relatively steep gradient under stronger SASM conditions during the late Holocene (e.g., 4,200 years BP to present) (note, Holocene subepoch boundaries follow Cohen et al. 2013, 2023) (Vuille and Werner, 2005; Vuille et al., 2012; Liu and Battisti, 2015). Accordingly, proxy records that reflect precipitation $\delta^{18}O$ values such as ice cores and speleothems have been used extensively to reconstruct the strength and geographic footprint of the SASM over the Holocene. For example, in the central Andes, ice core $\delta^{18}O$ records from Huascaran ice cap (9 °S; Figure 1b,2) (Thompson et al., 1995) and speleothem calcite $\delta^{18}O$ from Huagapo cave (11 °S; Figure 1b,2) (Kanner et al., 2013) closely track 11 °S insolation during the Holocene (Laskar et al., 2004), with the least negative $\delta^{18}O$ values (weakest SASM) corresponding with the early-Holocene summer insolation minimum and the most negative $\delta^{18}O$ values (strongest SASM) corresponding with peak summertime insolation in the late Holocene.

Precipitation $\delta^{18}O$ values in the tropics have also been interpreted as reflecting rainfall amount (i.e., the "amount effect") at the collection site, where there is an inverse relationship between precipitation amount and $\delta^{18}O$ value (Dansgaard, 1964). Although recent papers discuss the challenges with invoking the amount effect to interpret precipitation $\delta^{18}O$ values in the tropics (e.g., Konecky et al., 2019), for sites proximal to the Atlantic, there is some basis for relating local $\delta^{18}O$ to precipitation amount (Cruz et al., 2009; Liu and Battisti, 2015; Ward et al., 2019). However, this mechanism is not well-established in the central Andes despite modeling efforts (Vuille and Werner, 2005; Liu and Battisti, 2015), extensive modern precipitation data (Aron et al., 2021b), and paleoclimate records (Ward et al., 2019; Woods et al., 2020). Instead, some studies suggest SASM strength through the Holocene may have been decoupled from local moisture availability in the central Andes (Vuille and Werner, 2005; Ward et al., 2019; Woods et al., 2020). Therefore, in the central Andes, precipitation $\delta^{18}O$ values do not offer strong, quantitative evidence of past precipitation amount variations and provide little clarity as to how local *P–E* responds to global climate change.

Developing local *P–E* histories depends on records that are sensitive to changes in water balance, for example, lake levels and hydrology (e.g., Abbott et al., 1997; Placzek et al., 2006), glacier extent (e.g., Stansell et al., 2013, 2017; Sagredo et al., 2014) and faunal assemblages (e.g., Hansen et al., 1994; Rozas-Davila et al., 2023). One region that has been extensively studied is the Lake Junín region in the central Andes (approximately 10.5–11.5 °S; 75.5–76.5 °W; Figure 2). Specifically, pollen and sedimentological records from Lake Junín provide evidence of a shift from relatively dry conditions at the start of the Holocene (11,700 BP) to wet in the present (Hansen et al., 1994; Weidhaas, 2017; Woods, 2021; Rozas-Davila et al., 2023; Schiferl et al., 2023). Other studies have relied on isotopic records from Lake Junín to address *P–E* (Seltzer et al., 2000), as lake water $\delta^{18}O$ values increase with respect to precipitation $\delta^{18}O$ values under evaporated conditions and this signature is recorded by lake carbonate (e.g., Leng and Marshall, 2004; Gibson et al., 2016). In a widely cited study, Seltzer et al. (2000) compared the carbonate $\delta^{18}O$ from Lake Junín to the Huascaran ice core $\delta^{18}O$ record (which they interpret to more directly reflect precipitation $\delta^{18}O$) (Thompson et al., 1995) to estimate evaporative loss and observed a maximum offset between the two records in the early Holocene followed by a steady convergence towards present (Figure 1b). The authors attributed these results to a reduction in evaporative losses from the lake over the Holocene and increasingly wet conditions under strengthening SASM (Figure 1). Later studies replicate this approach by comparing the Lake Junín carbonate $\delta^{18}O$ record to a speleothem $\delta^{18}O$ record from Huagapo cave (Kanner et al., 2013) and to Pumacocha, a hydrologically open lake (Bird et al., 2011a), with similar interpretations of the Lake Junín $\delta^{18}O$ record across all three studies (Figure 1,2).

Although the Lake Junín $\delta^{18}O$ record is one of a handful of datasets frequently used as evidence of *P–E* change in the central Andes, interpretations based on $\delta^{18}O$ values rely on two assumptions. The first is that the Lake Junín carbonate $\delta^{18}O$ record reflects only changes in precipitation $\delta^{18}O$ values and evaporation, not other factors like temperature and hydrology, which are also known to affect carbonate $\delta^{18}O$ values (e.g., Leng and Marshall, 2004). Without methods to independently constrain temperature and lake water evaporation, the influence of these factors on carbonate $\delta^{18}O$ has never been directly tested. The second assumption is that $\delta^{18}O$ records from Huascaran ice core, Huagapo cave, and Pumacocha lake carbonates reflect only changes in precipitation $\delta^{18}O$ values and that differences in site location, elevation, and archive type are negligible. Studies that directly compare the different depositional settings could help establish the

relationship between $\delta^{18}O$ values recorded by lacustrine, cave, and ice archives, but parallel campaigns to monitor site conditions and/or proxy system modeling (e.g., Dee et al., 2015, 2018) have not yet been established. As a result, the timing and magnitude of *P–E* change in the Lake Junín region remains unclear.

In this study, we develop a framework to evaluate *P–E* change from lake records using carbonate clumped (Δ_{47}) and triple oxygen ($\Delta'^{17}O$) isotopes, which are proxies for the temperature of carbonate formation and degree of lake evaporation, respectively. We present new estimates of Holocene lake water evaporative states and temperature from Lake Junín in order to test longstanding interpretations of the carbonate $\delta^{18}O$ record. We also present evaporation and temperature records from Lakes Pumacocha and Mehcocha, two small, hydrologically open lakes today, which are assumed to track precipitation $\delta^{18}O$ values across the Holocene. Finally, using a lake water isotope mass balance model, we estimate hydrologic change in the three lakes and offer new insights into the Holocene *P–E* balance of the central Andes.

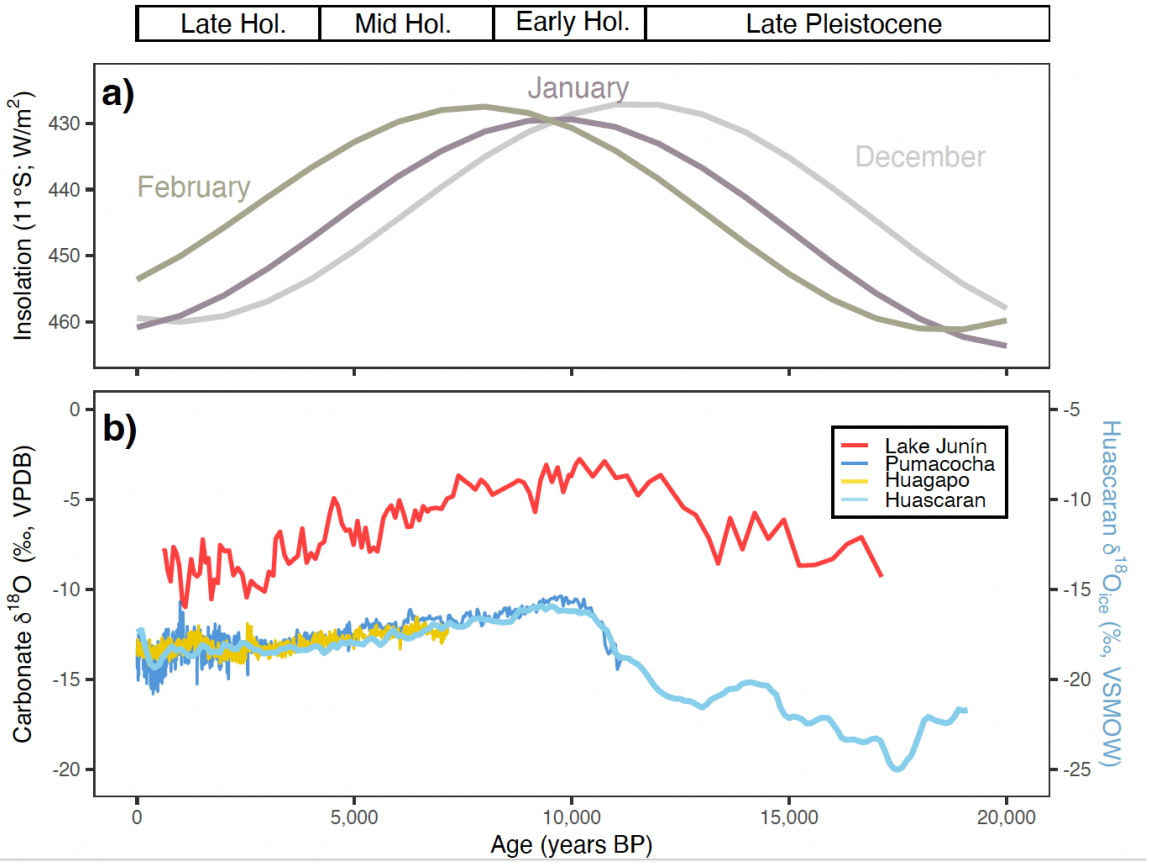

Figure 1: Summer insolation and hydroclimate records from the Lake Junín region and Cordillera Blanca (9–11 °S). (a) Summer (Dec–Feb) insolation at 11 °S calculated based on orbital solutions of Laskar et al. (2004) using the R package *palinsol* (Crucifix, 2016), with y-axis scale reversed. (b) Carbonate $\delta^{18}O$ records from Lake Junín (Seltzer et al., 2000), Lake Pumacocha (Bird et al., 2011a, 2011b), and Huagapo cave (Kanner et al., 2013). The Huascaran ice core $\delta^{18}O$ record is plotted on the right-hand y-axis (Thompson et al., 1995). Epoch and subepoch boundaries follow Cohen et al. (2013, 2023).

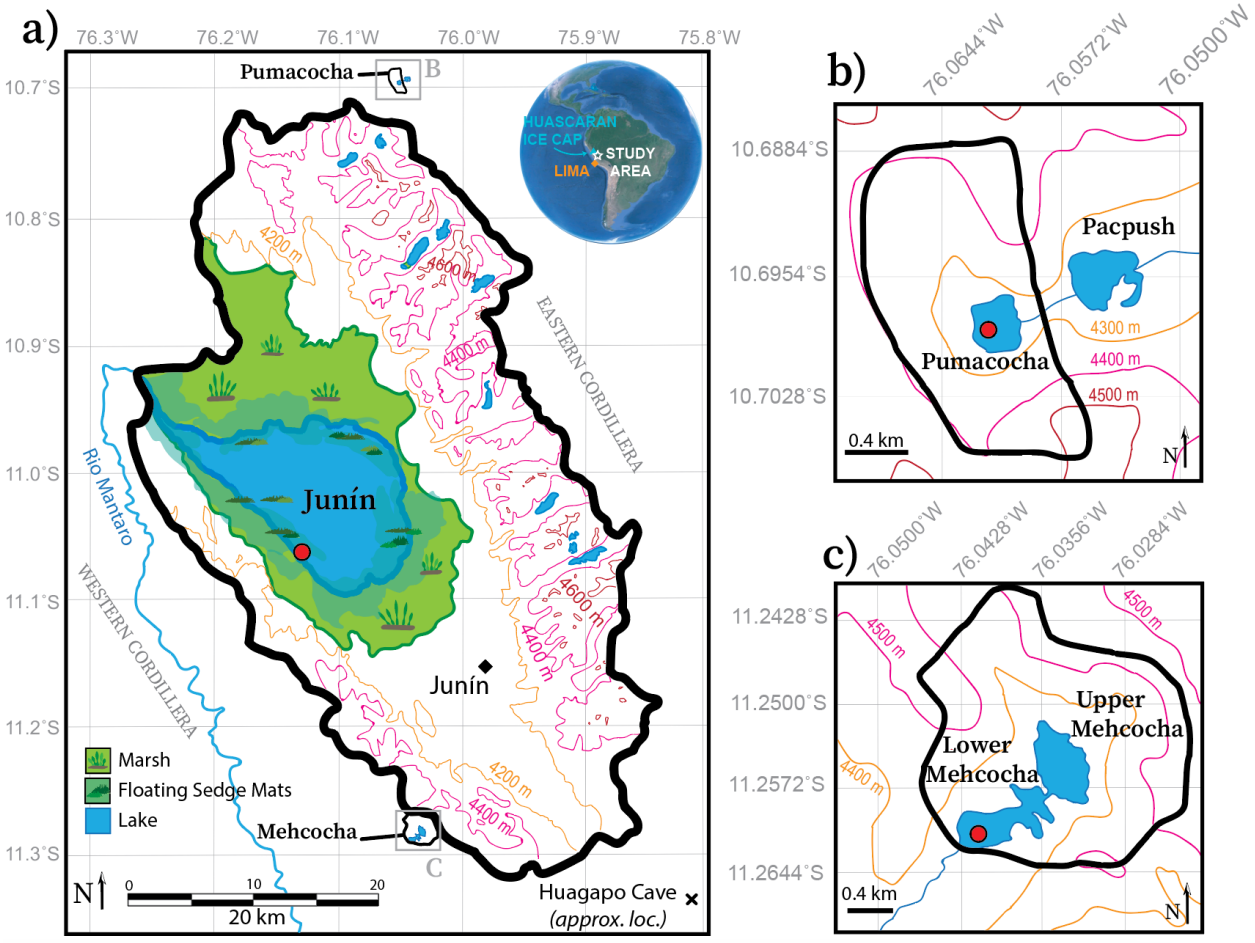

Figure 2: Maps of the three lake basins discussed in this study: (a) Junín, (b) Pumacocha, and (c) Mehcocha. Elevation contours shown at 200 m (a) and 100 m (b,c) intervals and thick black outlines denote the watershed boundaries. Red circles in each panel show the approximate coring location at each lake. Inset map in (a), modified from Google Earth, shows the location of the study area and other locations discussed in the text (Google LLC, 2022). Modified from Fig. 2 of Katz et al. (2023) and reprinted with permission of Elsevier.

2. Isotope Notation:

Isotope ratios are reported with respect to a standard in either "delta" (Eq. 1) or "delta prime" (Eq. 2) notation:

$$\delta^{X}O = ({}^{X}R_{sample}/{}^{X}R_{standard} - 1) \quad \text{Eq. 1}$$

$$\delta'^{X}O = \ln({}^{X}R_{sample}/{}^{X}R_{standard}) \quad \text{Eq. 2}$$

Where R represents the measured ratio of heavy to light isotopes and X is the atomic mass number of the heavy isotope. Both delta and delta prime values are reported in units of "per mil," ‰, where Equations 1 and 2 are multiplied by 10^3.

In a two-isotope system (e.g., $^{18}O/^{16}O$) fractionation between forms or phases (i.e., A, B) that contain the element of interest is expressed with the fractionation factor, α:

$$^{18}\alpha_{A-B} = \frac{^{18}R_A}{^{18}R_B} \quad \text{Eq. 3}$$

In a three-isotope system (e.g., $^{18}O/^{16}O$, $^{17}O/^{16}O$) fractionation factors among isotopologues are related by a power law (Matsuhisa et al., 1978; Young et al., 2002):

$$^{17}\alpha_{A-B} = \left(^{18}\alpha_{A-B}\right)^{\theta} \quad \text{Eq. 4}$$

Where θ represents a fractionation exponent for a discrete process such as water vapor diffusion (θ_{diff}) or equilibrium exchange (θ_{eq}). For processes that may be a combination of discrete fractionation steps, e.g., lake water evaporation, the term λ is used instead of θ (e.g., λ_{lake}).

The term $\Delta'^{17}O$ is defined as:

$$\Delta'^{17}O = \delta'^{17}O - \lambda_{ref} * \delta'^{18}O \quad \text{Eq. 5}$$

and commonly reported in units of "per meg" where Equation 5 is multiplied by 10^6. In hydrologic studies, the reference slope in $\delta'^{18}O$–$\delta'^{17}O$ space, λ_{ref}, is commonly defined as 0.528 (Luz and Barkan, 2010). This definition is useful in hydrologic studies because the liquid water–water vapor equilibrium fractionation exponent, $\theta_{eq} = 0.529$ (Luz and Barkan, 2005), is similar to λ_{ref}, such that λ_{ref} closely approximates the slope of Rayleigh processes and the slope of the Global Meteoric Water Line (≈ 0.528) (Luz and Barkan, 2010; Terzer-Wassmuth et al., 2023). Other processes, such as diffusion of water vapor through air, follow a shallower slope in $\delta'^{18}O$–$\delta'^{17}O$ space where $\theta_{diff} = 0.5185$ (Barkan and Luz, 2007). Evaporation involves both diffusion of water vapor and equilibrium liquid water–water vapor exchange, and the distinct θ_{diff} value leads to modification of the $\Delta'^{17}O$ values in water bodies that have experienced evaporative losses.

In carbonate materials formed in equilibrium with formation waters, the fractionation factor between water and calcite, $^{18}\alpha_{calcite\text{-}water}$, is temperature dependent (Kim and O'Neil, 1997). Carbonate "clumped isotopes" provide carbonate formation temperatures and can be used to constrain $\delta^{18}O$ values of formation water. The stochastic abundance of random "clumps," or bonds between two heavy isotopes, e.g., ^{13}C–^{18}O, can be predicted based on sample $\delta^{13}C$ and $\delta^{18}O$ values. However, in line with thermodynamic predictions, the measured abundance of "clumps" exceeds the stochastic abundance at Earth's surface conditions (Wang et al., 2004; Schauble et al., 2006). This difference, Δ_{47}, is inversely proportional to formation temperature and independent of sample $\delta^{13}C$ and $\delta^{18}O$ values. Δ_{47} can be defined as:

$$\Delta_{47} = \left[\left(\frac{R47}{R47^*} - 1\right) - \left(\frac{R46}{R46^*} - 1\right) - \left(\frac{R45}{R45^*} - 1\right)\right] \quad \text{Eq. 6}$$

where stochastic ratios are marked with "*". Clumped isotopes have been used to infer formation temperatures, $T\Delta_{47}$, from various types of natural carbonates, including lake carbonates spanning a broad range of climatic settings and hydrologic configurations (Huntington et al., 2010, 2015; Hren and Sheldon, 2012; Horton et al., 2016; Passey and Ji, 2019; Santi et al., 2020; Fetrow et al., 2022; Katz et al., 2023).

3. Foundation and interpretive framework:

3.1. Lake water balance

The water balance of lakes can be described as the volumetric proportion of inputs and losses to the lake basin. In most lakes, direct precipitation and catchment runoff constitute the primary inputs (I), while evaporation (E) and outflow (O) constitute the major losses (Figure 3).

Over a time interval of interest, the mass-balance of lakes can be described as a "steady state" system if the volumetric ratio of inputs equals losses:

$$I = E + O \quad \text{Eq. 7}$$

Likewise, steady state conditions also conserve the isotopic mass balance of lakes (Criss, 1999):

$$IR_I = ER_E + OR_O \quad \text{Eq. 8}$$

In a well-mixed lake, it is assumed that the isotopic composition of lake water, R_{lw}, equals R_O.

In this study, we group lakes into two hydrologic categories, open and closed, differentiated by the proportion of water loss via evaporation, relative to the total incoming water (Figure 3). The proportion of evaporation to inputs can be expressed numerically as X_E:

$$X_E = \frac{E}{I} \quad \text{Eq. 9}$$

Under this definition, closed basin lakes have X_E values of 1, reflecting a hydrologic endmember where all losses are via evaporation. Open lakes have X_E values <1 and have a portion of their water loss via outflow; they can be further differentiated as outflow-only ($X_E = 0$), outflow-dominated ($0 < X_E < 0.5$), and evaporation-dominated ($0.5 < X_E < 1$) (Figure 3).

Within a region of uniform climate conditions, lakes can exist along a hydrologic spectrum due to variability in basin (e.g., size, topography) and lake (e.g., surface area, depth) characteristics. Over time, changes in regional water balance will also drive hydrologic change among lakes; under more positive water balance conditions (i.e., "wetter") lakes will shift towards a greater proportion of inflow (lower X_E), whereas in negative water balance conditions lakes will shift towards a decreasing proportion of outflow (i.e., "drier," higher X_E).

The isotopic composition of lake water, R_{lw}, is highly sensitive to lake hydrology (i.e., X_E) (Herwartz et al., 2017; Gázquez et al., 2018; Passey and Ji, 2019) and can be calculated as:

$$R_{lw} = \frac{\alpha_{eq} R_I [\alpha_{diff}(1-h)+h(1-F)] + \alpha_{eq} h X_E R_A F}{X_E + \alpha_{eq}(1-X_E)\,[\alpha_{diff}(1-h)+h(1-F)]} \quad \text{Eq. 10}$$

Equation 10 (e.g., Benson and White, 1994; Passey and Ji, 2019) describes a steady state lake where α_{eq} is the temperature-dependent equilibrium exchange between water at the lake surface and atmospheric water vapor (Majoube, 1971) and α_{diff} is "diffusion" of lake water into the unsaturated atmosphere. For $^{18}O/^{16}O$, $^{18}\alpha_{diff}$ values can range between 1 (for non-fractionating, turbulent conditions) and 1.02849 (for molecular diffusion; Merlivat, 1978). Therefore, $^{18}\alpha_{diff}$ can be calculated as $^{18}\alpha_{diff} = 1.02849\Phi + (1 - \Phi)$, where Φ is the relative proportion of diffusive to turbulent transport of water vapor during evaporation (Passey and Ji, 2019). Relative humidity normalized to lake surface temperature is represented by h and F is the fraction of atmospheric vapor derived from distal sources versus the lake itself (where 1 and 0 represent exclusively distal and lake-derived sources of atmospheric vapor, respectively). Assuming that R_A, the isotopic ratio of atmospheric vapor, is in equilibrium with R_I, α_{eq} can be used to calculate R_A. However, note that this approach does not explicitly account for the effect of evaporation on R_A when $F < 1$, nor does it account for the possibility that atmospheric water vapor was derived from a different source or a mixture of sources (e.g., Aggarwal et al., 2016; Aron et al., 2021b).

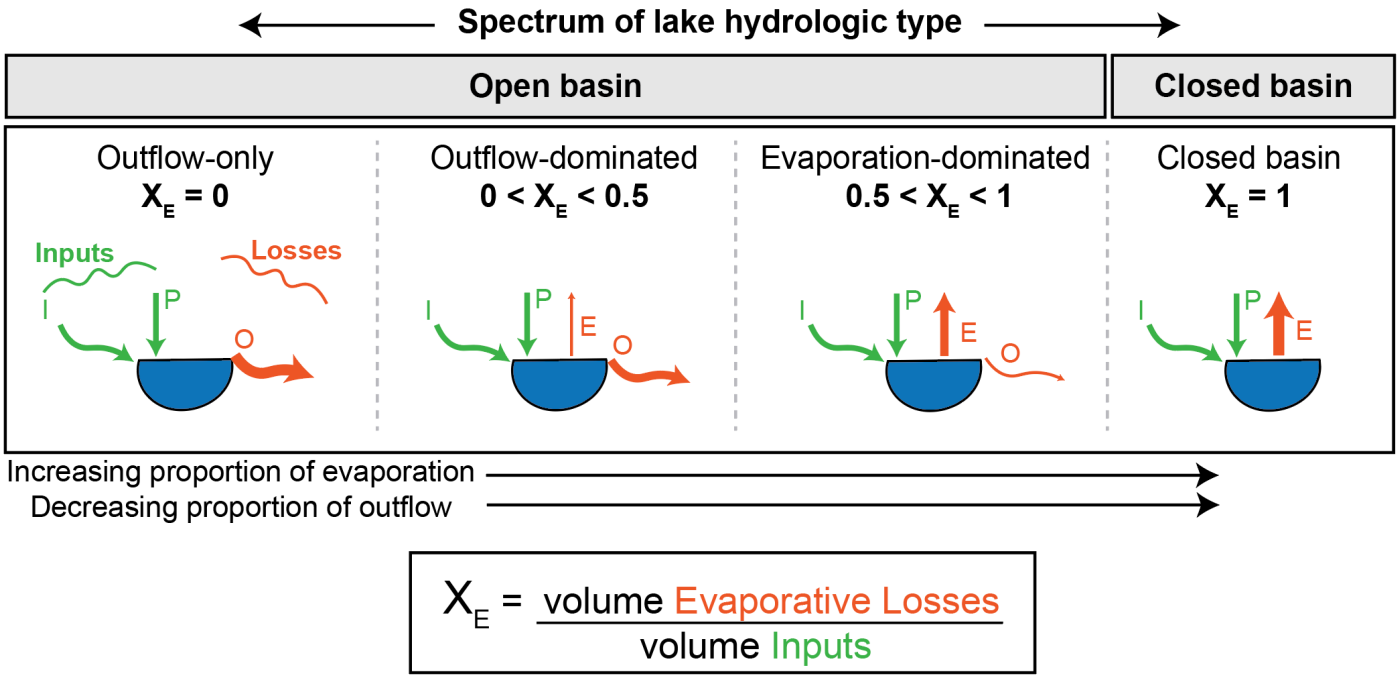

Figure 3: Schematic showing the spectrum of lake hydrology from open basin lakes to closed basin lakes. From left to right, the proportion of loss via evaporation and outflow increases and decreases, respectively. X_E is the volumetric proportion of evaporation (E) over inputs (I), see Equation 9 and associated text for more information.

3.2. **A system for interpreting lake carbonate isotope records**

Lake carbonate $\delta^{18}O$ records have been used to build hydroclimate records for many decades. However, the process of translating carbonate proxy data into information about past environmental conditions is rarely straightforward because carbonate $\delta^{18}O$ values can be influenced by precipitation dynamics, moisture source variation, lake water evaporation, and mineralization temperatures (Figure 4) (Leng and Marshall, 2004; Horton et al., 2016; Gibson et al., 2016). In this study, we explicitly account for lake temperature and evaporation using a multi-proxy isotope approach (i.e., Δ_{47}, $\Delta'^{17}O$; see Figure 4). This coupled hydrologic and isotope mass balance approach allows regional rainfall processes to be decoupled from local water balance (i.e., P–E) and temperature.

Figure 4a illustrates the two primary controls on the isotopic composition of lake waters: the isotopic composition of water entering the lake ($\delta^{18}O_I$) and evaporation (Leng and Marshall, 2004; Horton et al., 2016; Gibson et al., 2016). The relationship of these two variables to lake water $\delta^{18}O$ ($\delta^{18}O_{lw}$) values is shown by Equation 10 ($\delta^{18}O_{lw} = {}^{18}R_{lw}/{}^{18}R_{SMOW} - 1$). Logically, it makes sense that $\delta^{18}O_I$ values strongly influence $\delta^{18}O_{lw}$ values and that changing $\delta^{18}O_I$ values will translate to a corresponding change in $\delta^{18}O_{lw}$ values (Figure 4b). Principally, $\delta^{18}O_I$ reflects water cycle processes on a regional scale and is strongly related to upwind processes including Rayleigh distillation or conditions at the moisture source (Dansgaard, 1964; Gat, 1996). Unlike $\delta^{18}O$, Rayleigh distillation has little effect on $\Delta'^{17}O$ values of precipitation (Figure 4b) (Aron et al., 2021a).

Lake waters can also experience evaporation, which selectively removes light isotopes into the unsaturated atmosphere while heavy isotopes become concentrated in the remaining lake water (Figure 4c). As a result, evaporated $\delta^{18}O_{lw}$ values are higher compared to $\delta^{18}O_I$ values (Figure 4c) (Leng and Marshall, 2004; Horton et al., 2016; Gibson et al., 2016). Lake water $\Delta'^{17}O$ values

become lower compared to input water as the slope of evaporation in $\delta'^{18}O$–$\delta'^{17}O$ space is lower than λ_{ref} (e.g., Gázquez et al., 2018; Passey and Ji, 2019). In hydrologically open lakes where X_E approaches 0 and evaporation is not a significant water balance component, $\delta^{18}O_{lw}$ values will be close to $\delta^{18}O_I$. As the role of evaporation increases (i.e., as X_E increases), so too will the isotopic offset of $\delta^{18}O_{lw}$ and $\delta^{18}O_I$ (Figure 4c). Similarly, $\Delta'^{17}O_{lw}$ is closest to $\Delta'^{17}O_I$ when X_E approaches 0 and is much lower than $\Delta'^{17}O_I$ when $X_E >> 0$ (Figure 4c) (Gázquez et al., 2018; Katz et al., 2023).

For ancient lake systems, we often lack information about $\delta^{18}O_I$ and/or evaporation, so it is difficult to understand how each component individually contributes to $\delta^{18}O_{lw}$ values (Leng and Marshall, 2004). However, because $\Delta'^{17}O$ is highly sensitive to evaporation but is relatively insensitive to Rayleigh processes (Figure 4b,c), it is an ideal tool to constrain lake hydrologic balance and has been successfully applied to a number of modern and paleo lake systems (Herwartz et al., 2017; Gázquez et al., 2018; Passey and Ji, 2019; Ibarra et al., 2021; Voigt et al., 2021; Katz et al., 2023).

Another challenge in studying ancient lake systems is that ancient lake water cannot be measured directly, therefore, we must instead rely on isotope records from authigenic minerals that track changes in $\delta^{18}O_{lw}$ values (Figure 4). Carbonate $\delta^{18}O$ ($\delta^{18}O_C$) values are related to $\delta^{18}O_{lw}$ values by the temperature dependent fractionation factor ($^{18}\alpha_{calcite\text{-}water}$) (Kim and O'Neil, 1997) which can be determined from carbonate clumped isotope formation temperatures ($T\Delta_{47}$) (Figure 4d). Together, the combination of $\delta^{18}O_C$ and $T\Delta_{47}$ can be used to constrain $\delta^{18}O_{lw}$ values and to develop surface temperature records from lacustrine sediments (Huntington et al., 2010, 2015; Hren and Sheldon, 2012; Horton et al., 2016; Passey and Ji, 2019; Santi et al., 2020; Fetrow et al., 2022; Katz et al., 2023).

When used in tandem, $\delta^{18}O$, $T\Delta_{47}$, and $\Delta'^{17}O$ can be used to develop more robust hydroclimate records that improve upon interpretations based only on carbonate $\delta^{18}O$ values (Figure 4) (Passey and Ji, 2019; Katz et al., 2023). In Sections 7.1 and 7.2, we apply new $T\Delta_{47}$ and $\Delta'^{17}O$ data to this framework to evaluate the temperature and hydrologic influences on carbonate $\delta^{18}O$ records from Lakes Junín, Pumacocha, and Mehcocha.

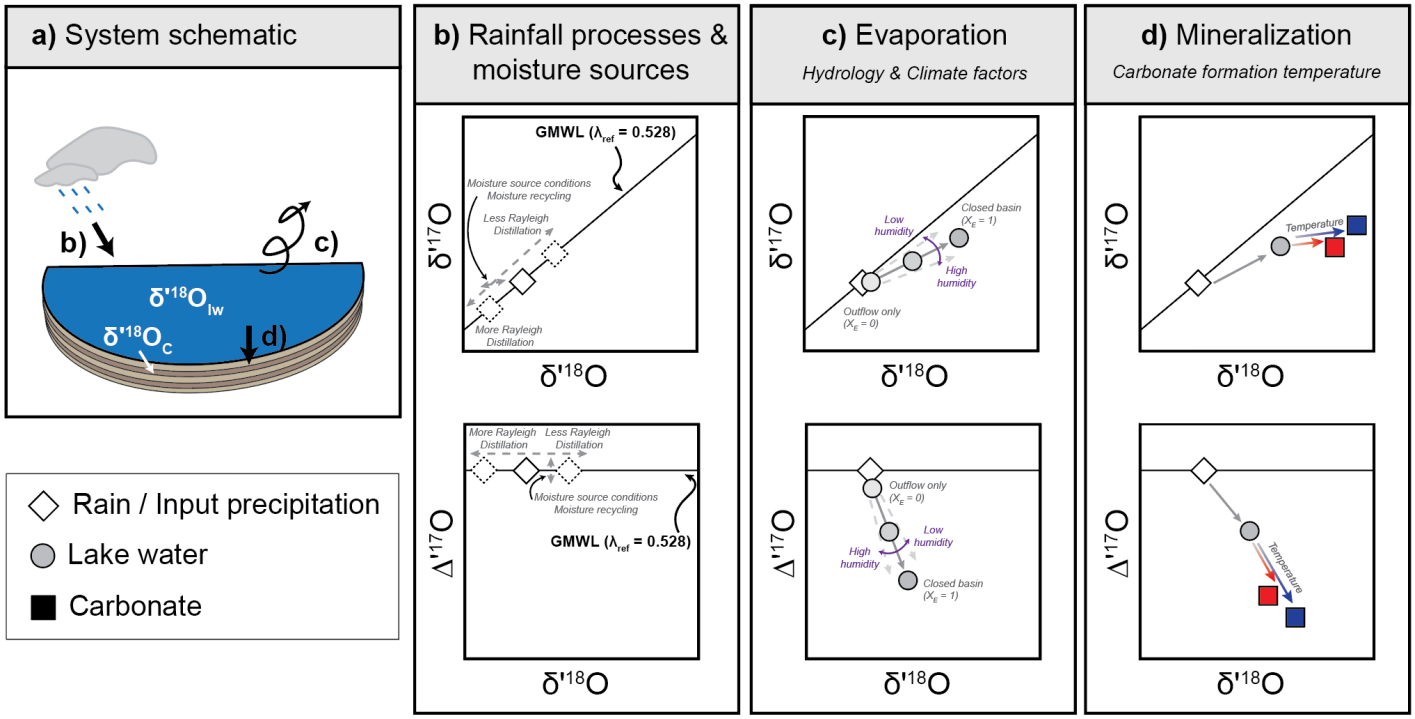

Figure 4: (a) Schematic representing three important processes that influence the isotopic compositions of lake water ($\delta'^{18}O_{lw}$) and carbonates ($\delta'^{18}O_C$): (b) rainfall processes and moisture source conditions, (c) evaporation, and (d) mineralization. Note: not to scale.

4. Study area:

4.1. Regional climate and geologic overview:

The Lake Junín region in the Andean Cordillera sits at an elevation of >4,000 meters above sea level (masl) (Figure 2). Mean annual air temperature in the region is 6.5 °C and diurnal temperature swings (ca. 0–15 °C) greatly exceed variations in average monthly temperatures. Modern precipitation is highly seasonal; ~70% of annual precipitation (900–1,000 mm) occurs in October–April during the strengthened phase of the SASM (Garreaud et al., 2009; Marengo et al., 2012; SENAMHI, 2023). Annual potential evapotranspiration is 525–550 mm/year and relative humidity is consistently 70–90% (SENAMHI, 2023; Katz et al., 2023). The three study lakes are all located in the upper headwaters of the Amazon Basin. Outflow from Lakes Junín and Mehcocha enter Rio Mantaro, and Pumacocha feeds Rio Huachón (Figure 2); eventually, these rivers converge in the Andean foothills and feed the Amazon River in northeast Peru.

Bedrock in the Lake Junín region is primarily Triassic–Jurassic aged marine carbonate from the Pucará Group with some exposure of Permian sandstones (Mitu Group) and Carboniferous carbonates and sandstones (Tarma and Ambo Groups; Ministerio de Energia y Minas, 1979b, 1979a, 1979c; Cobbing et al., 1996). High bicarbonate concentrations in surface waters results in carbonate production in many lakes throughout the region (Flusche et al., 2005).

4.2. Lake Junín:

Lake Junín is located north of Junín, Peru on a high elevation plateau (4,080 masl, Figure 2a). Alluvial fans and glacial outwash form the northern boundary of the basin and prominent Pleistocene glacial moraines are present east of the lake (Hansen et al., 1994; Seltzer et al., 2000; Smith et al., 2005; Woods et al., 2020; Rodbell et al., 2022).

Lake Junín covers a large, ~300 km^2, surface area that represents approximately one third of the total catchment area (Seltzer et al., 2000; Woods et al., 2020). Maximum water depth is 8-12 m, such that the lake surface area to volume ratio is high (~125:1). Accordingly, the lake is highly sensitive to both evaporative water losses and outflow via the Rio Mantaro (Figure 2–3,4c). Precipitation, runoff from the catchment, and groundwater springs along the southwest shore constitute the major volumetric inputs to Lake Junín (Flusche et al., 2005). Directly downstream of Lake Junín, a hydroelectric dam has modified natural lake hydrology since the 1930s, however, we expect that under modern precipitation and climate conditions, lake hydrology would remain open throughout the year, though could become seasonally closed basin during the winter dry season. Despite these fluctuations, the lake can be considered in steady-state on interannual timescales.

The sediment core used in this study was collected from Lake Junín in 1996 at the western margin of the lake (Figure 2a). The top 11 meters of the core are composed of laminated marl which was analyzed for carbonate $\delta^{18}O$ by Seltzer et al., (2000) and reflects continuous sedimentation over the last 21,200 years, based on radiocarbon dating.

4.3. Lake Pumacocha:

Pumacocha is located ~40 km northeast of Junín in the eastern Andean Cordillera. The small, deep lake (Figure 2a,b; surface area: 0.1 km^2; depth: 23.5 m; elevation: 4,300 masl) fills a glacial cirque. Pumacocha's lake surface area to volume ratio, ~42:1, is much lower than at Lake Junín. The major water balance components of the lake are precipitation, catchment runoff, and outflow. Today the ratio of evaporation to inputs in this system is very low (Bird et al., 2011b, 2011a), such that X_E is close to 0 and the lake is hydrologically open basin (Figure 3, see Section 3.1, 4.5).

Sediment cores from Pumacocha were collected between 2005–2008 and analyzed for carbonate $\delta^{18}O$ values by Bird et al. (2011b, 2011a). Core age models date the base of the core to ~10,000 years BP and were determined by a combination of ^{137}Cs, varve counting, and radiocarbon dates (Bird et al., 2011b, 2011a). Authigenic carbonate and bands of organic material are present throughout the core and glacial clays are present at the base, representing the formation of the lake post-Holocene deglaciation (Bird et al., 2011a).

4.4. Lake Mehcocha:

The formal name for this lake is Catucana, but we use an informal name, "Mehcocha," here for consistency with prior studies (e.g., Katz et al., 2023). Mehcocha is located ~12 km southwest of Junín in the western Andean Cordillera (elevation: 4,355 masl). The catchment is composed of two sub-basins which are connected by a narrow straight (Figure 2c). The total surface area for both sub-basins is 0.2 km^2 and maximum water depths are 25.5 m and 12.4 m in the upper and lower sub-basins, respectively. Similar to Pumacocha, Mehcocha has a low surface area to volume ratio at ~50:1. The primary water balance components are precipitation, catchment runoff, and outflow; evaporation is low and the lake is an open basin with X_E near 0 (Figure 3, see Section 3.1). Construction of a road during historical times modified the natural lake outflow, but we assume this had negligible impacts to lake hydrology.

In 2015, stratigraphically overlapping sediment cores were collected from two locations in the lower sub-basin using a lance-driven piston corer deployed from a floating platform on the lake surface. We focus our analyses on core C-15, which was collected from a water depth of 12.4 m, spans 10.1 m of stratigraphy, and terminates on a gravelly-clay glacial till unit that confirms

complete recovery of the postglacial sequence. Holocene sediments at this site are predominantly low density (~0.2 g/cm^3), organic-rich (organic matter weight percent values from ~20% to ~60%), dark brown to brown, banded muds with intervening units of coarse carbonate sand and shell fragments.

4.5. Prior hydroclimate interpretations based on carbonate $\delta^{18}O$

The three lakes in this study represent a range of open basin hydrologic configurations, as defined in Section 3.1, from outflow-only at Pumacocha and Mehcocha to outflow-dominated at Lake Junín (Figure 3). Consistent with the framework outlined in Section 3.2, the modern lake water isotope composition reflects both the isotopic composition of input waters and hydrology (i.e., X_E; Figure 4). Specifically, input and lake water isotope values are most similar under low evaporation conditions and become dissimilar as evaporation leads to enrichment of heavy isotopes in lake water. Modern lake waters at Pumacocha and Mehcocha have $\delta^{18}O$ and $\Delta'^{17}O$ values identical to mean annual precipitation, consistent with outflow-only lakes as shown in Figure 4b,c (Bird et al., 2011b, 2011a; Katz et al., 2023). Lake Junín lake water $\delta^{18}O$ and $\Delta'^{17}O$ values are higher and lower, respectively, than mean annual precipitation due to evaporation (Figure 4c) (Flusche et al., 2005; Katz et al., 2023).

Previous workers have leveraged these differences in modern hydrology when interpreting the Holocene carbonate $\delta^{18}O$ records from these lakes. At Pumacocha, carbonate $\delta^{18}O$ values decreased steadily from ca -10 ‰ in the early Holocene to ca -15 ‰ (VPDB) in the late Holocene ($\delta^{18}O_{late}$–$\delta^{18}O_{early}$ = -5 ‰; Figure 5b) (Bird et al., 2011b, 2011a). This trend is interpreted as a decrease in $\delta^{18}O_I$ values by the same magnitude caused by an insolation-driven increase in SASM strength over the last 10,000 years (Bird et al., 2011a). To a first order, this interpretation is consistent with the steady decrease in $\delta^{18}O$ values observed both at the nearby Huagapo Cave (from -14 to -11 ‰ VPDB; $\delta^{18}O_{late}$–$\delta^{18}O_{early}$ = -3 ‰) (Kanner et al., 2013) and Huascaran ice core (from -19 to -16 ‰, VSMOW; $\delta^{18}O_{late}$–$\delta^{18}O_{early}$ = -3 ‰) (Thompson et al., 1995), which reflects increasing SASM convective activity (Figure 1). Lake hydrology and temperature are not thought to influence the carbonate $\delta^{18}O$ trend (Figure 4), and it is assumed Pumacocha remained open basin through the Holocene (Figure 3,4). However, these assumptions have not been tested by isotopic approaches that can independently resolve changes in lake hydrology, temperature, and input $\delta^{18}O$ values (i.e., Section 3.2, Figure 4).

Unlike Pumacocha, the influence of evaporation on both modern lake water balance and isotopic composition is well-documented at Lake Junín (Section 3; Figure 3,4) (Flusche et al., 2005; Katz et al., 2023). Compared to the Holocene records from Pumacocha, the Lake Junín carbonate $\delta^{18}O$ record is higher by +7 ‰ in the early Holocene before steadily decreasing to +2 ‰ higher in the late Holocene (Figure 5b) (Seltzer et al., 2000; Bird et al., 2011b, 2011a). In previous studies, the offset was entirely attributed to a decreasing proportion of evaporative loss from the lake and increasingly positive water balance (i.e., P–E) associated with increasing SASM strength over the Holocene (Figure 3,4) (Seltzer et al., 2000; Bird et al., 2011b, 2011a; Kanner et al., 2013). Accordingly, this interpretation implies local water balance is in-sync with global climate drivers (i.e., insolation). However, these interpretations have relied on the assumption that the $\delta^{18}O$ offset between Lake Junín and other records only reflects changes in local P–E and they hypothesize that other factors that can affect carbonate or ice $\delta^{18}O$ values, including temperature or local basin dynamics, were minimal relative to the effects of evaporation (Figure 4) (Kanner et al., 2013; Bird et al. 2011; Seltzer et al., 2000), which is sometimes at odds with the original interpretation of the records (Thompson et al., 1995).

5. Laboratory methods and data processing:

5.1. Radiocarbon dating and age models

We present an updated Bayesian age model for the Lake Junín core (Figure S1–S2; Table S1–S3) based on a combination of the radiocarbon dates presented by Seltzer et al. (2000) and 11 new radiocarbon dates. We also present radiometric dates (Table S4) and a Bayesian age model (Figure S3–S4; Table S5–S6) for the Mehcocha sediment core. Additional methodological information related to radiocarbon dating and age models is provided in Text S1.

5.2. Analytical preparation for Δ_{47} and $\Delta'^{17}O$ analysis:

We sampled the lake cores from Lakes Junín, Pumacocha, and Mehcocha at approximately 1,000–1,200 year intervals from the start of the Holocene (11,700 years BP) to the present (Table 1). Two additional samples were selected from Lake Junín during the latest Pleistocene (17,210 and 12,870 years BP; Table 1). To the greatest degree possible, the Holocene samples were collected from contemporaneous time intervals to facilitate direct comparison among the three lakes.

Bulk sediment samples were treated overnight with 7% hydrogen peroxide to remove organic matter via oxidation. Sediment was then rinsed through a 63 μm mesh, retaining the <63 μm size fraction for isotopic analysis. Samples were dried at 50 °C for several days. A mortar and pestle were used to homogenize sediment prior to analysis. The processed material is light colored (ranging from white to light grey) and void of macroscopic shell or plant materials. In some samples, the process yielded insufficient carbonate material for analysis.

5.3. Isotope analyses:

5.3.1. Carbonate Clumped Isotopes:

Carbonate clumped isotope measurements were made at the University of Michigan (UM) Isotopologue Paleosciences Lab (IPL). We follow the approach described by Passey et al. (2010). To summarize this procedure, carbonate first is digested in a common acid bath containing >100 wt% phosphoric acid at 90 °C, producing CO_2 and H_2O. The latter is trapped cryogenically (via a water trap held at -78 °C) and after passing through this first trap, CO_2 is collected in a second trap held at liquid nitrogen temperature (-180 °C). After isolating the purified CO_2, the sample is thawed and passed through a gas chromatograph held at ca. -20 °C (via a He carrier gas) to further purify the sample before recollection on a final trap held at liquid nitrogen temperature. The high purity CO_2 gas is then introduced to a Nu Perspectives isotope ratio mass spectrometer for analysis in dual inlet mode. Sample gas was measured 40 times (50 second integration; *m/z* 44–49) and laboratory working gas was measured before and after each sample measurement. From these measurements, we calculate $\delta^{13}C$, $\delta^{18}O$ and Δ_{47} values versus laboratory working gas using Brand/IUPAC parameters (Petersen et al., 2019).

Data corrections are performed using a mixed correction of both equilibrium CO_2 gases and carbonate standards run within the same analytical session as samples. Equilibrium gas standards of two distinct $\delta^{13}C$ and $\delta^{18}O$ compositions were introduced to the same sample prep line as used for carbonate samples. Low temperature equilibrated gases were thermally equilibrated in a 30 °C water bath. High temperature equilibrated (i.e., "heated") gases were generated "on-line" from the same equilibrated gas reservoirs, but with the gases being passed through a furnace held at 1000 °C immediately prior to analysis (upstream of the gas chromatograph cleanup step) to produce a stochastic distribution of ^{13}C-^{18}O bonds. We also

analyzed carbonate ETH (ETH1-4) and IAEA (IAEA-C1 and IAEA-603) standards using the same in-line sample preparatory line and following the same procedure as for samples. Carbonate $\delta^{13}C$ and $\delta^{18}O$ values were standardized to the VPDB reference frame using known values of ETH1-4 (Bernasconi et al., 2018) and IAEA reference materials (assuming IAEA-C1 is isotopically identical to IAEA-603) (Assonov et al., 2020). Measured Δ_{47} data were projected to absolute values ($\Delta_{47\ ICDES90}$) following the approach of Daëron et al. (2016) using measurements of equilibrium gases and ETH1-3 carbonate standards. Finally, we plotted residual Δ_{47} values of ETH4, IAEA-C1, and IAEA-603 from accepted values to assess and correct for in-session offsets and drift.

5.3.2. Triple Oxygen Isotopes:

Triple oxygen isotope measurements were made at the UM IPL. We use a three-step process to convert carbonate to O_2 as outlined by Passey et al. (2014) and Ellis and Passey (2023). First, carbonate is digested in H_3PO_4 in a common acid bath at 90 °C and resultant CO_2 is purified using the same approach as described above for clumped isotopes (e.g., digestion biproducts are removed cryogenically and by passage through a GC column) (Passey et al., 2010). Next, CO_2 undergoes methanation to produce H_2O. This is accomplished by reacting CO_2 with excess H_2 over an Fe catalyst held at 560 °C. Lastly, the H_2O is transferred via He carrier gas through a cobalt trifluoride reactor (CoF_3, 360 °C). The O_2 analyte produced by fluorination is purified via gas chromatography and cryogenic separation prior to introduction to a Nu Perspective isotope ratio mass spectrometer. Sample analysis consists of 40 measurements of sample and reference gas, with each gas measurement consisting of a 50 second integration over an *m/z* range of 32–36.

Samples were analyzed concurrently with water standards VSMOW2 and SLAP2, and carbonate standards IAEA-C1 and an in-house groundwater carbonate standard (102-GC-AZ01). Data normalization is carried out over the lifetime of each cobalt trifluoride reactor (replaced every ~200 analyses) with VSMOW2 and SLAP2 typically run in the beginning, middle, and end of each reactor. Sample data are first normalized to the VSMOW-SLAP scale as outlined by Schoenemann et al. (2013; $\delta^{18}O_{VSMOW}$= 0.000 ‰; $\delta^{18}O_{SLAP2}$= -55.500 ‰; $\Delta'^{17}O_{VSMOW}$ and $\Delta'^{17}O_{SLAP2}$ = 0 per meg) and a linear drift correction is applied across the reactor. This yields normalized values for an O_2 analyte. To determine $\Delta'^{17}O$ values of carbonate, we assign $\Delta'^{17}O$ values of IAEA-C1 to the values reported by Wostbrock et al. (2020) (-100 per meg) following methods outlined in Huth et al. (2022).

6. Results:

Mehcocha carbonate $\delta^{13}C$ and $\delta^{18}O$ values range from -3.4 to 0.6 ‰ and -14.1 to -9.8 ‰, respectively (VPDB) (Table S6, Figure 5, S3–S4).

Carbonate clumped isotope data, $\delta^{13}C$, $\delta^{18}O$, Δ_{47}, are reported in Tables 1 and S7. Carbonate $\delta^{18}O$ data are also shown in Figure 5b. Clumped isotope formation temperatures ($T\Delta_{47}$ values) were calculated from Δ_{47} values using Equation 1 of Anderson et al. (2021) and range from 3.7 to 14.9 °C across all lakes (Table 1, S7; Figure 5c).

Carbonate triple oxygen isotope data, $\delta'^{17}O$, $\delta'^{18}O$, $\Delta'^{17}O$, are reported in Tables 1 and S8. Carbonate $\delta'^{18}O$ and $\Delta'^{17}O$ values at Pumacocha and Mehcocha range from 16.5 to 19.7 ‰ and -88 to -63 per meg (VSMOW-SLAP) and at Lake Junín range from 19.0 to 28.2 ‰ and -82 to -107 per meg (VSMOW-SLAP), respectively.

We also calculated reconstructed lake water $\delta'^{18}O$ and $\Delta'^{17}O$ ($\delta'^{18}O_{rlw}$; $\Delta'^{17}O_{rlw}$) values (Table 1, S7). $\delta'^{18}O_{rlw}$ values were calculated from carbonate $\delta^{18}O$ values using $^{18}\alpha_{calcite\text{-}water}$ (Kim

and O'Neil, 1997) and temperatures derived from Δ_{47} values. $\delta'^{18}O_{rlw}$ values at Pumacocha and Mehcocha range from -14.9 to -11.7 ‰ and at Lake Junín range from -12.1 to -3.9 ‰ (VSMOW; Figure 5d). $\Delta'^{17}O_{rlw}$ values were calculated using a $\lambda_{calcite\text{-}water}$ value of 0.5250 (Huth et al., 2022). $\Delta'^{17}O_{rlw}$ values at Pumacocha and Mehcocha are 6 to 30 per meg and at Lake Junín are -13 to 11 per meg (VSMOW-SLAP; Table 1; Figure 5e).

Propagated uncertainty was calculated for both $\delta'^{18}O_{rlw}$ and $\Delta'^{17}O_{rlw}$ values using a Monte Carlo resampling approach. For $\delta'^{18}O_{rlw}$ values, the average and 1 σ standard error of $\delta^{18}O_C$ and $T\Delta_{47}$ values (calculated from replicate analyses) were used to resample 10,000 values for both populations; new $^{18}\alpha_{calcite\text{-}water}$ values were calculated from $T\Delta_{47}$ values and applied to $\delta^{18}O_C$ values to determine $\delta'^{18}O_{rlw}$ values. The 1 σ standard deviation of the resampled $\delta'^{18}O_{rlw}$ population is reported in Table 1. The propagated uncertainty for $\Delta'^{17}O_{rlw}$ was calculated similarly using the $\Delta'^{17}O_C$ and $\delta'^{18}O_C$ values from triple oxygen isotope analyses and $T\Delta_{47}$ values (Table 1; Figure 5E).

546 Table 1: Sample information and summarized carbonate isotope data from Lakes Junín, Pumacocha, and Mehcocha

				Derived from clumped isotopes										Derived from triple oxygen isotopes							
Sample ID	**Comp Depth (cm)**	**Age (yr BP)**	**No. rep. Δ_{47} / $\Delta'^{17}O$ anal.**	**$\delta^{13}C_C$ (‰, VPDB)**	**$\delta^{13}C_C$ 1σ SD (‰)**	**$\delta^{18}O_C$ (‰, VPDB)**	**$\delta^{18}O_C$ 1σ SD (‰)**	**Δ_{47} ICDES90 (‰)**	**Δ_{47} ICDES90 1σ SD (‰)**	**$T\Delta_{47}$ (°C) †**	**$T\Delta_{47}$ 1σ SD (°C)**	**$\delta'^{18}O_{rlw}$ ‡ (‰, VSMOW)**	**$\delta'^{18}O_{rlw}$ # 1σ SD (‰)**	**$\delta'^{17}O_C$ (‰, VSMOW -SLAP)**	**$\delta'^{17}O_C$ 1σ SD (‰)**	**$\delta'^{18}O_C$ (‰, VSMOW -SLAP)**	**$\delta'^{18}O_C$ 1σ SD (‰)**	**$\Delta'^{17}O_C$ (per meg; VSMOW -SLAP)**	**$\Delta'^{17}O_C$ 1σ SD (per meg)**	**$\Delta'^{17}O_{rlw}$ & (per meg; VSMOW -SLAP)**	**$\Delta'^{17}O_{rlw}$ * 1σ SD (per meg)**
Junín (11.05 °S, 76.12 °W, 4080 masl)																					
Junín D4 10.0-15.0 cm	110	1134	3 / 2	4.760	0.054	-10.812	0.026	0.637	0.008	11.4	2.4	-11.361	0.307	9.943	0.504	18.986	0.962	-82	4	11	3
Junín D5 30.0-35.0 cm	230	2299	4 / 2	5.317	0.111	-9.343	0.049	0.651	0.016	7.4	4.4	-10.790	0.505	10.862	0.070	20.749	0.132	-93	0	2	2
Junín D6 10.0-15.0 cm	310	3322	4 / 2	7.022	0.100	-7.362	0.050	0.657	0.016	5.6	4.6	-9.201	0.532	12.526	0.073	23.913	0.121	-100	9	-3	7
Junín D7 8.0-13.0 cm	408	4536	3 / 2	11.023	0.064	-5.476	0.053	0.638	0.018	11.1	5.1	-6.050	0.650	13.427	0.145	25.633	0.263	-107	6	-14	5
Junín D8 30.0-35.0 cm	530	5923	4 / 2	11.398	0.137	-5.963	0.059	0.650	0.021	7.8	6.0	-7.303	0.686	13.272	0.013	25.333	0.029	-104	2	-9	3
Junín D9 30.0-35.0 cm	630	7241	4 / 2	13.212	0.062	-4.793	0.047	0.649	0.015	7.9	4.3	-6.098	0.491	13.750	0.194	26.245	0.379	-108	5	-12	4
Junín D10 7.0-12.0 cm	724	8762	3 / --	13.710	0.115	-4.243	0.028	0.643	0.016	9.6	4.5	-5.159	0.583	--	--	--	--	--	--	--	--
Junín D10 78.0-83.0 cm	795	9912	4 / 2	14.149	0.103	-3.597	0.044	0.634	0.017	12.4	5.1	-3.886	0.559	13.995	0.592	26.704	1.117	-105	2	-13	2
Junín D11 10.0-15.0 cm	810	10276	4 / 1	15.510	0.171	-2.906	0.055	0.646	0.023	9.0	6.6	-3.959	0.734	14.792	--	28.211	--	-104	--	-9	--
Junín D11 88.0-93.0 cm	888	12873	3 / 2	11.912	0.039	-5.253	0.092	0.664	0.009	3.7	2.3	-7.536	0.313	13.020	0.314	24.852	0.598	-102	2	-4	2
Junín D12 91.0-96.0 cm	991	17214	3 / 2	3.792	0.017	-10.350	0.042	0.655	0.010	6.1	2.7	-12.104	0.359	11.025	0.052	21.054	0.104	-92	2	5	2
Pumacocha (10.699 °S, 76.061 °W, 4300 masl)																					
Pumacocha A-05 D2 38.75 cm	124.25	1243	3 / 4	-3.186	0.009	-13.864	0.107	0.636	0.010	11.8	2.9	-14.365	0.370	8.643	0.150	16.487	0.288	-63	5	30	3
Pumacocha A-05 D3 49.65 cm	195.85	2495	2 / 2	-3.253	0.000	-13.362	0.148	0.640	0.007	10.4	2.0	-14.173	0.327	9.120	0.876	17.400	1.658	-67	1	26	1
Pumacocha A-05 D5 26.25 cm	283.35	3522	3 / 2	-3.220	0.026	-13.110	0.108	0.649	0.009	7.9	2.6	-14.476	0.343	9.328	0.192	17.791	0.353	-66	6	30	4
Pumacocha A-05 D6 11 cm	340.70	4528	3 / 3	-3.119	0.015	-13.017	0.133	0.633	0.006	12.6	1.8	-13.338	0.241	9.092	0.579	17.361	1.099	-75	11	17	6
Pumacocha E-06 D3 38.75 cm	398.45	5892	4 / 3	-2.600	0.059	-12.502	0.076	0.638	0.021	11.1	6.2	-13.145	0.675	9.719	0.307	18.551	0.588	-75	4	18	3
Pumacocha E-06 D3 76.75 cm	436.45	7133	3 / 4	-2.221	0.024	-11.903	0.054	0.625	0.007	14.9	2.0	-11.707	0.250	9.825	0.238	18.768	0.452	-84	8	6	4
Pumacocha E-06 D4 59.25 cm	515.55	9363	4 / 3	-2.232	0.050	-10.682	0.064	0.648	0.016	8.4	4.6	-11.919	0.521	10.306	0.166	19.658	0.309	-73	4	21	3

Table 1, continued.

				Derived from clumped isotopes										Derived from triple oxygen isotopes							
Sample ID	**Comp Depth (cm)**	**Age (yr BP)**	**No. rep. Δ_{47} / $\Delta'^{17}O$ anal.**	**$\delta^{13}C_C$ (‰, VPDB)**	**$\delta^{13}C_C$ 1σ SD (‰)**	**$\delta^{18}O_C$ (‰, VPDB)**	**$\delta^{18}O_C$ 1σ SD (‰)**	**Δ_{47} ICDES90 (‰)**	**Δ_{47} ICDES90 1σ SD (‰)**	**$T\Delta_{47}$ (°C) †**	**$T\Delta_{47}$ 1σ SD (°C)**	**$\delta'^{18}O_{rlw}$ ‡ (‰, VSMOW)**	**$\delta'^{18}O_{rlw}$ # 1σ SD (‰)**	**$\delta'^{17}O_C$ (‰, VSMOW -SLAP)**	**$\delta'^{17}O_C$ 1σ SD (‰)**	**$\delta'^{18}O_C$ (‰, VSMOW -SLAP)**	**$\delta'^{18}O_C$ 1σ SD (‰)**	**$\Delta'^{17}O_C$ (per meg; VSMOW -SLAP)**	**$\Delta'^{17}O_C$ 1σ SD (per meg)**	**$\Delta'^{17}O_{rlw}$ & (per meg; VSMOW -SLAP)**	**$\Delta'^{17}O_{rlw}$ * 1σ SD (per meg)**
Mehcocha (11.255 °S, 76.035 °W, 4355 masl)																					
Mehcocha C-15 D2 15 cm	115	1238	3 / 2	-2.728	0.232	-13.756	0.028	0.641	0.013	10.2	3.8	-14.624	0.484	8.662	0.098	16.543	0.196	-73	6	21	4
Mehcocha C-15 D4 33 cm	333	3524	3 / 2	-2.085	0.051	-13.732	0.074	0.646	0.009	8.9	2.6	-14.897	0.337	8.722	0.060	16.653	0.105	-70	4	24	3
Mehcocha C-15 D6 23 cm	523	5884	3 / 2	-1.619	0.202	-12.484	0.032	0.644	0.017	9.3	4.8	-13.532	0.616	9.307	0.048	17.781	0.091	-81	1	13	2
Mehcocha C-15 D7 55 cm	655	7101	-- / 1	--	--	--	--	--	--	--	--	--	--	8.943	--	17.103	--	-88	--	7 §	--
Mehcocha C-15 D8 35 cm	735	9350	-- / 2	--	--	--	--	--	--	--	--	--	--	9.724	0.126	18.560	0.229	-76	5	18 §	--

547

† Calculated using Anderson et al., 2021, Equation 1.

‡ Calculated from $\delta^{18}O_C$ and $^{18}\alpha_{calcite\text{-}water}$ derived from $T\Delta_{47}$ from Kim and O'Neil, 1997.

Propagated uncertainty based on clumped isotope $\delta^{18}O_C$ and $T\Delta_{47}$ values.

& Calculated from $\delta^{18}O_C$ and $\delta^{17}O_C$ values derived from triple oxygen isotope analysis and using $\lambda_{calcite\text{-}water} = 0.5250$ (Huth et al., 2022).

§ Calculated assuming a formation temperature of 9 °C.

* Propagated uncertainty based on $\Delta'^{17}O_C$ and $T\Delta_{47}$ values.

548

549

550

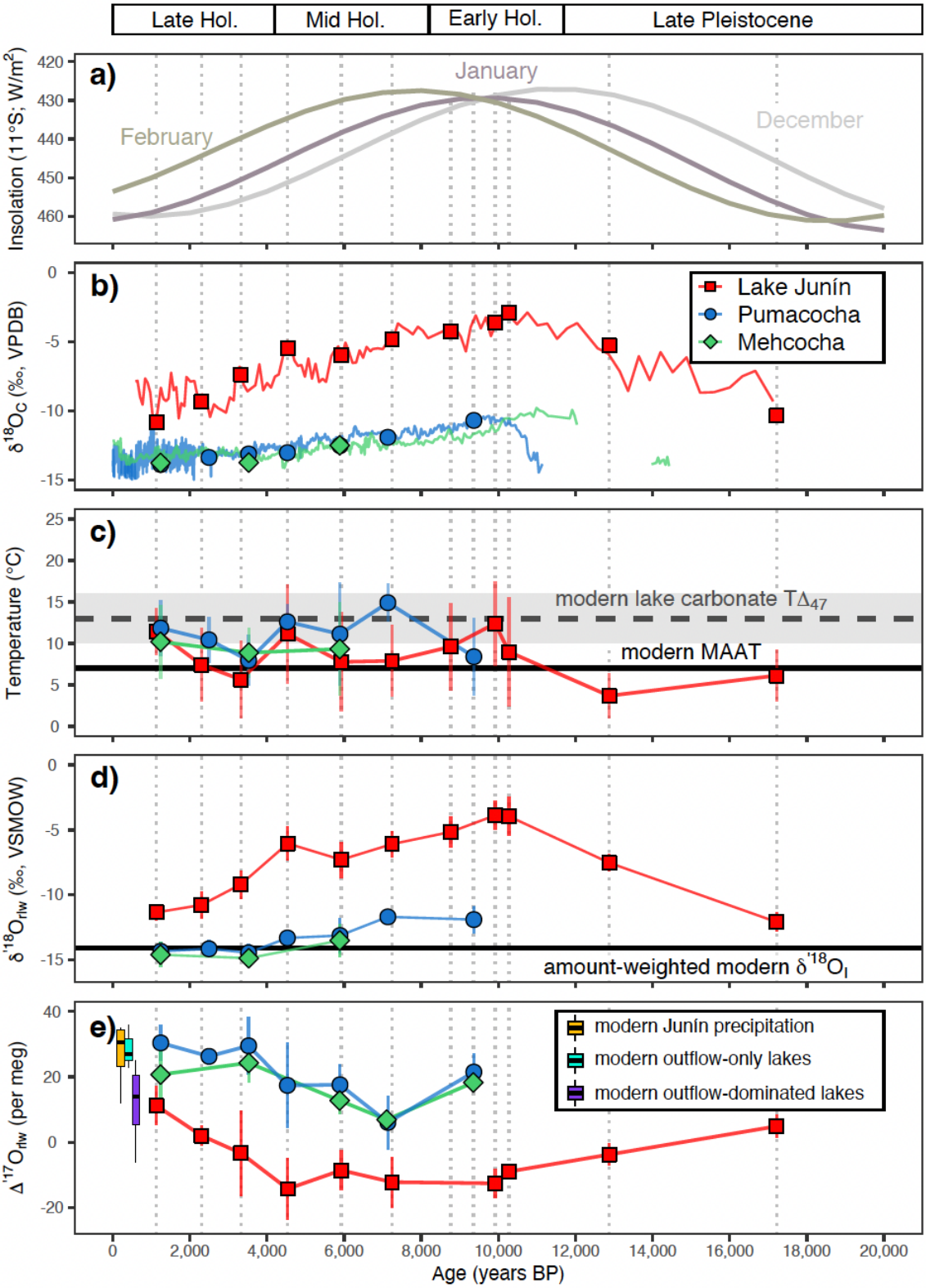

551
552 Figure 5: (a) As in Figure 1a, Summer (Dec–Feb) insolation at 11 °S (Laskar et al., 2004; Crucifix, 2016), with y-
553 axis scale reversed. (b) As in Figure 1b, carbonate $\delta^{18}O$ records from Lakes Junín (red; Seltzer et al., 2000),

Pumacocha (blue; Bird et al., 2011a,b), Mehcocha (green). Symbols represent carbonate $\delta^{18}O$ values derived from Δ_{47} analysis. (c) Reconstructed formation temperatures from lake carbonate Δ_{47} values. Error bars represent 2σ SE of replicate analyses. Solid black and dashed grey horizontal lines, respectively, show mean annual air temperature (MAAT; 6.5 °C) and modern lake carbonate $T\Delta_{47}$ values for these lakes (13 ± 3 °C), for reference (Katz et al., 2023). (d) Reconstructed lake water $\delta'^{18}O$ ($\delta'^{18}O_{rlw}$) derived from carbonate clumped isotope $\delta^{18}O$ and $T\Delta_{47}$ values; error bars represent 2σ SD propagated uncertainty. Black horizontal line shows modern $\delta'^{18}O$ inputs ("amount-weighted modern $\delta'^{18}O_I$"; Katz et al., 2023) from local amount-weighted mean annual precipitation, for reference. (e) Reconstructed lake water $\Delta'^{17}O$ calculated from carbonate $\Delta'^{17}O$, $T\Delta_{47}$, and $\lambda_{calcite\text{-}water} = 0.5250$, Huth et al. (2022); error bars represent 2σ SD propagated uncertainty. Box and whisker plots (in the style of Tukey) show the $\Delta'^{17}O$ range of modern precipitation (yellow), outflow-only lakes (teal; Pumacocha and Mehcocha), and outflow-dominated lakes (purple; Lake Junín) in the Lake Junín region (water data from Katz et al., 2023). Note, some samples were unable to be analyzed for both Δ_{47} and $\Delta'^{17}O$ due to limited material, such that more points are shown in panel (e) than in panels (b)–(d). In panels (a)–(e), dotted grey vertical lines align with sample dates to facilitate comparison between plots. Data from Table 1.

7. Discussion:

7.1. Lake water temperatures and the influence on carbonate $\delta^{18}O$ values:

The results of our clumped isotope analysis show that the reconstructed Holocene water temperature records are indistinguishable among the three lakes within analytical precision (Figure 5c). Water temperatures (10 ± 2 °C, n = 19) were stable over the Holocene and are similar to water temperatures derived from clumped isotopes of modern lacustrine carbonates from the same lakes (13 ± 3 °C; Figure 5c; Table 1) (Katz et al., 2023). Carbonate $T\Delta_{47}$ values from Lake Junín in the latest Pleistocene (17,210 and 12,870 years BP) are 5 ± 2 °C (n = 2), and suggest that water temperatures were cooler by ~5 °C (Figure 5c; Table 1). This may suggest that local air temperatures were lower during the latest Pleistocene or that cool glacial melt waters were entering the lake from the surrounding catchment.

The relatively constant $T\Delta_{47}$ values indicate that changes in Holocene water temperature is not the primary driver of the observed carbonate $\delta^{18}O$ trend at any of the lakes. Additionally, temperature changes are not responsible for the offsets observed among the different records (Figure 5b). $\delta^{18}O_{rlw}$ values for each of the three lakes thus show similar patterns to carbonate $\delta^{18}O$ values (Figure 5b,d). This suggests that, consistent with prior interpretations of these records (see Section 4.5), effects other than temperature, for example, changes in input rainfall $\delta^{18}O$ values (Figure 4b) and/or evaporation (Figure 4c), drive the decrease in carbonate $\delta^{18}O$ at all three lakes over the Holocene.

7.2. Hydrologic interpretations based on $\Delta'^{17}O$

Evaporation is one of several processes that influence the isotopic composition of lake waters (e.g., Leng and Marshall, 2004; Gibson et al., 2016) and can be used to infer local P–E conditions through its link to lake water balance (Eq. 9,10; Section 3.2; Figures 3,4). In this section, we use reconstructed lake water $\Delta'^{17}O$ ($\Delta'^{17}O_{rlw}$) values from Lakes Junín, Pumacocha, and Mehcocha to first establish the role of evaporation on the $\delta^{18}O_{rlw}$ records from these lakes following our interpretive framework described in Section 3.2. Then we use $\Delta'^{17}O_{rlw}$ values to model changes in lake water balance (i.e., X_E). Finally, we show that when the $\Delta'^{17}O$–derived water balance records from these lakes are considered in unison, they illuminate changes in local P–E during the Holocene.

7.2.1. Pumacocha and Mehcocha

Based on prior interpretation of the Pumacocha record and the similarity of the Mehcocha $\delta^{18}O$ record and basin characteristics (see Section 4.5) (Bird et al., 2011b, 2011a), we expect that both lakes maintained an open, outflow-only hydrology through the Holocene and that $\Delta'^{17}O_{rlw}$ values from these lakes will be similar to $\Delta'^{17}O$ values of modern day precipitation in the region (31 ± 5 per meg; Figure 4a,b) (Katz et al., 2023). $\Delta'^{17}O_{rlw}$ values at Pumacocha and Mehcocha are consistent with these expectations during the late Holocene, with average values of 29 (± 2 per meg; n = 3) and 24 per meg (± 3 per meg; n = 2), respectively (Figure 5e). These results suggest that both lakes did maintain open hydrologic conditions (X_E close to 0) and that $\delta^{18}O_{rlw}$ values reflect $\delta^{18}O_I$ values in the late Holocene (4,200 years BP to present).

However, throughout the early and mid-Holocene (11,700–4,200 years BP), $\Delta'^{17}O_{rlw}$ values were significantly lower at both Pumacocha (16 ± 6 per meg, n = 4) and Mehcocha (12 ± 6 per meg, n = 3) (Figure 5e, Table 1). These data suggest that both lakes maintained open hydrology, but experienced greater evaporation in the early and mid-Holocene than the late Holocene. Three lines of reasoning support this interpretation: First, the two lake records match each other exceptionally well and show simultaneous, identical changes in $\Delta'^{17}O_{rlw}$ values (Figure 5e). Given the hydrologic similarities of the two lakes today, it makes sense that water balance of these lakes would respond similarly to climatic pressures in the past, such as local P–E changes. Secondly, the lowest $\Delta'^{17}O$ values correspond with the highest $\delta'^{18}O$ values (Figure S6), which is consistent with evaporative enrichment of waters (Figure 4b). Third, there is substantial evidence (isotopic and non-isotopic) that the central Andes was highly water-stressed in the early and mid-Holocene (discussed further in Section 7.3), and therefore it is unsurprising that lakes in this region would experience hydrologic change during this period. With respect to the $\delta^{18}O_{rlw}$ values at Pumacocha and Mehcocha throughout the early and mid-Holocene (Figure 5d), our $\Delta'^{17}O$ results suggest that $\delta^{18}O_{rlw}$ may be slightly higher than local $\delta^{18}O_I$ values at this time.

An alternative explanation for the low $\Delta'^{17}O_{rlw}$ values observed in the early and mid-Holocene is that $\Delta'^{17}O_I$ values were lower than the present (31 ± 5 per meg) (Katz et al., 2023). For global precipitation datasets today, there is a very small negative correlation between $\Delta'^{17}O$ and $\delta'^{18}O$ values (Terzer-Wassmuth et al., 2023); if such trends applied during the early to mid-Holocene, a 3‰ increase in $\delta'^{18}O_I$ values would correspond with $\Delta'^{17}O_I$ values <5 per meg lower. Other processes, such as sub-cloud evaporation or a change in the seasonality of precipitation could also result in slightly lower $\Delta'^{17}O_I$ values (≤ 10 per meg lower) (Aron et al., 2023; Terzer-Wassmuth et al., 2023). However, this change in $\Delta'^{17}O_I$ is insufficient to explain the full magnitude of $\Delta'^{17}O_{rlw}$ change observed at Pumacocha and Mehcocha, so lake water evaporation must contribute to at least part of the $\Delta'^{17}O_{rlw}$ trend. For the remainder of our analysis, we assume that local $\Delta'^{17}O_I$ values remained at 31 per meg throughout the Holocene. However, changes in $\Delta'^{17}O_I$ must be considered and we address this in Section 7.2.3.

Together, these $\Delta'^{17}O$ data suggest that both Pumacocha and Mehcocha maintained open hydrologic conditions throughout the Holocene, consistent with previous interpretations. However, during the early to mid-Holocene, local P–E conditions were drier and waters from both lakes experienced greater evaporation, contrasting with how isotopic records from these lakes were previously interpreted (Bird et al., 2011b, 2011a).

7.2.2. Lake Junín

The influence of evaporation on Lake Junín's water budget is well-established, both in the present (e.g., Flusche et al., 2005; Katz et al., 2023) and throughout the Holocene (Figure 3; see

Section 4.5) (Seltzer et al., 2000). Accordingly, we expect that Holocene $\Delta'^{17}O_{rlw}$ values will be lower than modern precipitation in the region (31 ± 5 per meg) (Katz et al., 2023) and will be the lowest in the early Holocene (11,700 to 8,200 years BP) when SASM was weakest and carbonate $\delta^{18}O$ values are highest (Figure 5a,b).

Our results show that all $\Delta'^{17}O_{rlw}$ values from Lake Junín are lower than modern precipitation $\Delta'^{17}O$ values (Figure 5e). Compared to Pumacocha and Mehcocha, the Lake Junín $\Delta'^{17}O_{rlw}$ record follows the same trend with time, though the $\Delta'^{17}O_{rlw}$ values are lower and exhibit a larger amplitude of change at Lake Junín (Figure 5e). This suggests that evaporation has always been a significant water balance component at Lake Junín (i.e., in agreement with the original carbonate $\delta^{18}O$ interpretation by Seltzer et al. (2000)), and that Pumacocha and Mehcocha maintained less-evaporated states, even as all three lakes responded to the same climate pressures. This is consistent with the differences in basin configuration among the lakes, as Lake Junín is the largest and shallowest of the three lakes, therefore water balance/lake hydrology is most likely to vary significantly with local climate.

The highest $\Delta'^{17}O_{rlw}$ values at Lake Junín are observed at 1,130 years BP (11 per meg) and 17,210 years BP (5 per meg) while the lowest $\Delta'^{17}O_{rlw}$ values (-14 to -9 per meg) are observed from 10,280 to 4,540 years BP (Figure 5e, Table 1). Variation in $\Delta'^{17}O_{rlw}$ values track the $\delta^{18}O_{rlw}$ values closely (Figure 5d,e); the strong negative correlation between $\Delta'^{17}O_{rlw}$ and $\delta^{18}O_{rlw}$ values (Figure S6) suggests that evaporation is the primary driver of the low $\Delta'^{17}O_{rlw}$ values at Lake Junín (Figure 4c). These data indicate that following peak evaporative conditions through the early and mid-Holocene (11,700 to 4,200 years BP), water balance began to steadily increase during the late Holocene before reaching an evaporative minimum in the present (Figure 4,5e).

We can evaluate the influence of evaporation on $\delta^{18}O_{rlw}$ values by comparing them to reconstructed unevaporated $\delta^{18}O_I$ values that we calculate from $\Delta'^{17}O_{rlw}$ and $\delta^{18}O_{rlw}$ values, using the approach of Passey and Ji (2019) as also done by others (Ibarra et al., 2021; Kelson et al., 2022; Katz et al., 2023; see Text S2). This approach allows us to assess whether changes in the degree of lake water evaporation accompanied changes in $\delta^{18}O_I$ values (i.e., due to changes in the SASM). The large differences in $\delta^{18}O_{rlw,}$ compared to reconstructed $\delta^{18}O_I$ values, shows that most of the variation in $\delta^{18}O_{rlw}$ values (and by extension $\delta^{18}O_C$ values) is due to evaporation (Figure S7; Table S9). However, we note that evaporation does not explain all the variation in reconstructed $\delta^{18}O_I$ values; the reconstructed $\delta^{18}O_I$ values are highest in the early to mid-Holocene when summer insolation is low and they reach minima when summer insolation is high, suggesting a connection to the SASM, consistent with interpretation of other $\delta^{18}O$ records from the region (e.g., Kanner et al., 2013). These data also indicate that the influence of evaporation on $\delta^{18}O_{rlw}$ values was greatest when SASM was weak (during the early to mid-Holocene), and vice versa, pointing to a probable connection between SASM and water balance, which was previously hypothesized (Seltzer et al., 2000), but couldn't be independently shown prior to this study. These results highlight the power of $\Delta'^{17}O$ for resolving evaporative histories in a way that cannot be accomplished by $\delta'^{18}O$ values alone.

7.2.3. Estimating lake water balance from $\Delta'^{17}O$ values and implications for P–E

The $\Delta'^{17}O_{rlw}$ results from Lakes Junín, Pumacocha, and Mehcocha record variable lake water evaporation over the Holocene that accompanied changes in the hydrology (X_E) of each lake. To investigate the potential relationship between hydrologic change and local *P–E*, we use a

deterministic approach to model the relationship between X_E and $\Delta'^{17}O_{rlw}$ values using Equation 10 (e.g., Benson and White, 1994; Passey and Ji, 2019) and the parameters listed in Table 2.

In Figure 6, we depict the modeled solution space under a normalized relative humidity (h) range of 0.1–0.9. We express $\Delta'^{17}O$ as the difference between lake water and input $\Delta'^{17}O$ values (i.e., $\Delta'^{17}O_{rlw} - \Delta'^{17}O_I$) and assume $\Delta'^{17}O_I$ is 31 per meg, consistent with modern precipitation in this region. Due to the multivariate nature of Equation 10, the modeled results create a wedge-like structure where $\Delta'^{17}O_{rlw}$ is closely related to both X_E and h (Figure 6) (e.g., Gázquez et al., 2018; Passey and Ji, 2019; Katz et al., 2023). We note that while altering the exact parameter values used in the model would induce some minor changes in the solution space, the overall trends between h, X_E, and $\Delta'^{17}O$ are conserved and this does not have a significant effect on our results. We provide code in the Supplemental Materials (Text S3) so that users can tailor model input values to match other study locations.

We use this model to estimate water balance during two intervals: the late Holocene and the early through mid-Holocene (Figure 6). Late Holocene average $\Delta'^{17}O_{rlw}$ values are calculated for Pumacocha and Mehcocha over the last 4,200 years when $\Delta'^{17}O_{rlw}$ values were relatively high and stable, and evaporation was at a minimum. For Lake Junín, $\Delta'^{17}O_{rlw}$ values are more variable during the late Holocene, so we only averaged $\Delta'^{17}O_{rlw}$ values over the last 2,500 years (e.g. the youngest two samples analyzed) to assess X_E during a relative evaporative minimum. Early to mid-Holocene $\Delta'^{17}O_{rlw}$ values are calculated as the average $\Delta'^{17}O_{rlw}$ from 4,200 to 11,700 years BP for each of the lakes when evaporation was at a maximum. Assuming that local humidity in the late Holocene was similar to present (0.7–0.83), we estimate X_E at Lake Junín was 0.4–0.7, reflecting an outflow or evaporation-dominated lake system, whereas both Pumacocha and Mehcocha functioned as outflow-only lakes, similar to today (Figure 3,6a). However, during the early and mid-Holocene (Figure 6b), X_E was between 0.5–1 at Lake Junín, indicative of evaporation-dominated hydrology or potentially closed basin conditions if humidity was similar to modern (~0.75). At Pumacocha and Mehcocha, X_E was between 0.2–0.3, suggesting these lakes maintained an outflow-dominated hydrology, but also experienced significant evaporation of up to 30% loss by volume (Figure 6b). Accounting for the sensitivity of X_E to $\Delta'^{17}O_I$, our conclusions are not substantially altered when a slightly lower $\Delta'^{17}O_I$ value is considered (see Section 7.2.1; Figure S8).

Evaluating lake hydrology across the Holocene, it is clear that all three lakes experienced a synchronous shift towards less evaporated conditions beginning during the late Holocene (after 4,200 years BP). The fact that this shift occurs concurrently at all three sites suggests it does not merely reflect the dynamics of a single lake, rather it likely reflects a regional shift towards more positive (i.e., wetter) P–E conditions. These results unambiguously point to the importance of P–E change on regional hydroclimate and on the $\delta^{18}O$ records from each of these lakes.

Table 2. Values used in deterministic modeling of Equation 10.

Variable	Value	Notes
$^{18}\alpha_{eq}$	1.010328	Calculated from Eq. 1 of Majoube (1971) and a temperature of 14 °C
$^{17}\alpha_{eq}$	1.00545	Calculated from $^{18}\alpha_{eq}$ using $\theta_{eq} = 0.529$
$^{18}\alpha_{diff}$	1.014245	Calculated using $\Phi = 0.5$
$^{17}\alpha_{diff}$	1.007361	Calculated from $^{18}\alpha_{diff}$ using $\theta_{diff} = 0.5185$
F	0.9	Estimated based on typical F estimates used for other lakes; selecting the higher end of the range used for the Great Lakes (0.6–0.9), assuming the smaller fetch of the Junín region lakes would lead to higher F values (Jasechko et al., 2014)
$^{18}R_I$	0.001977125	Calculated assuming $\delta'^{18}O_I = -14.1$ ‰
$^{17}R_I$	0.0003770939	Calculated from $^{18}R_I$ assuming a $\Delta'^{17}O_I$ value of 31 per meg
$^{18}R_A$	0.001954931	Calculated using $^{18}\alpha_{eq}$ and assuming vapor is in equilibrium with water of $\delta'^{18}O = -15$ ‰
$^{17}R_A$	0.0003748506	Calculated from $^{18}R_A$ assuming vapor is in equilibrium with water of $\Delta'^{17}O = 35$ per meg

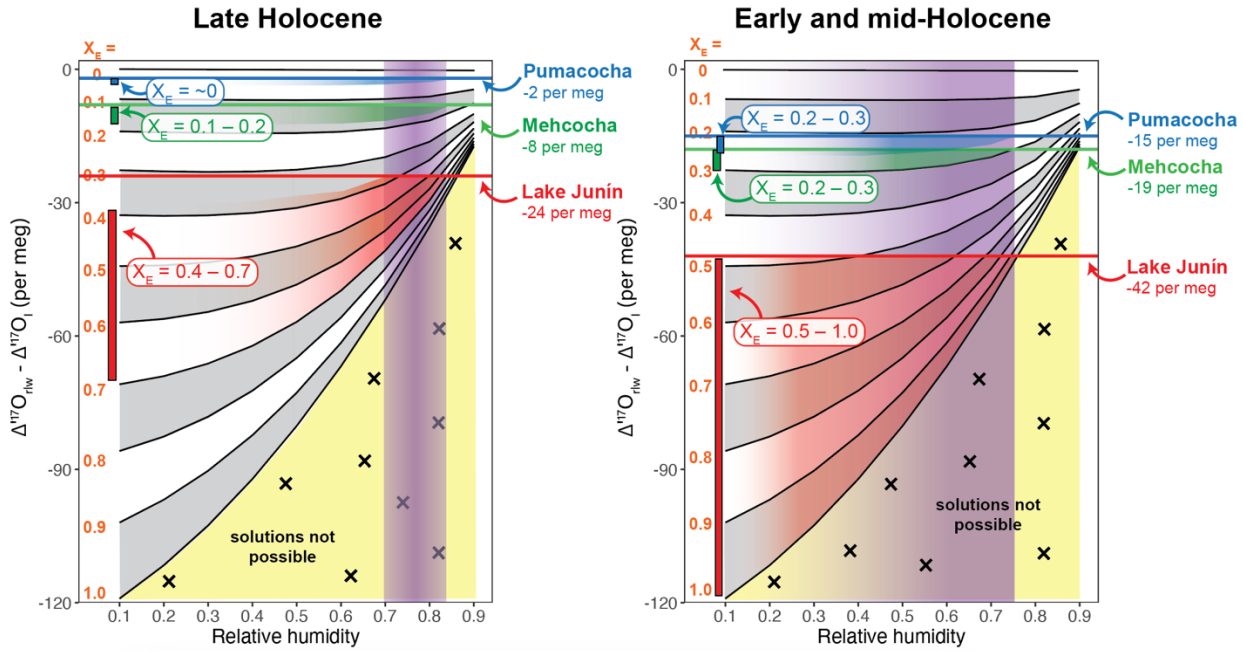

Figure 6: Deterministic model of Equation 10 using the values given in Table 2 under an X_E range from 0–1 and an h range of 0.1–0.9. $\Delta'^{17}O$ is shown as the difference between reconstructed lake water ($\Delta'^{17}O_{rlw}$) and input waters ($\Delta'^{17}O_I$ =31 per meg) where lower values correspond to greater evaporation. Orange text indicates modeled X_E and alternating white/grey wedges are shown to illustrate how $\Delta'^{17}O_{rlw}$–$\Delta'^{17}O_I$ and h vary over X_E increments of 0.1. Panels (a) and (b) show measured $\Delta'^{17}O_{rlw}$–$\Delta'^{17}O_I$ values as colored horizontal lines and X_E estimates as colored vertical bars for Lakes Junín (red), Pumacocha (blue), and Mehcocha (green) during the late Holocene and early through mid-Holocene, respectively. In (a), the vertical purple box shows the typical humidity range for this region in the present day (~0.7–0.83; SENHAMI, 2023; Katz et al., 2023). In (b), the purple box indicates the humidity range possible given both the model space and $\Delta'^{17}O_{rlw}$–$\Delta'^{17}O_I$ values for Lake Junín. The region shaded yellow indicates a $\Delta'^{17}O_{rlw}$–$\Delta'^{17}O_I$ and h space where solutions are not possible under the model conditions.

7.3. Placing local hydroclimate variability within a regional–global context

7.3.1. Holocene and late Pleistocene temperatures

South American temperature estimates from the Holocene are relatively sparce, but evidence from groundwater noble gases in the Amazon basin (Stute et al., 1995), pollen assemblages in the Bolivian foothills (Punyasena et al., 2008), and glacial equilibrium line elevations in the Junín region (Smith et al., 2005) suggest local temperatures were stable and similar to present. Global temperature estimates have also been derived from marine data assimilations and the reanalysis products suggest global temperature was relatively stable over the last 9,500 years and varied on the order of ~0.5 °C (Figure 7) (Osman et al., 2021). In comparison to Holocene temperatures, the marine proxies suggest global mean temperature was ~5–7 °C cooler during the Last Glacial (Figure 7) (Osman et al., 2021). The distribution of glacial features in the central Peruvian Andes also suggests terrestrial temperatures were cooler by ~5 °C during the Last Glacial and latest Pleistocene (Wright, 1983; Smith et al., 2005).

Within the analytical uncertainty of our results, the $T\Delta_{47}$ data from the Lake Junín region are consistent with other proxy records that suggest cooler regional surface temperatures by ~5 °C during the latest Pleistocene (Wright, 1983; Smith et al., 2005; Osman et al., 2021). During the Holocene, relatively constant temperatures that are similar to modern are observed (Figure 7) however the analytical uncertainty of our $T\Delta_{47}$ data (~2–5 °C) is large compared to the small magnitude of temperature change modeled for the South American monsoon region during the Holocene (~1 °C; e.g., Hancock et al., 2023) which means that we are unable to definitively assess whether temperature changes of this magnitude (i.e., 1 °C) occurred at our study sites. Low sampling resolution inhibits us from resolving regional temperature change on sub-millennial timescales, however, our data suggest that local temperatures stabilized at near-modern conditions by around 10,000 years BP. Overall, these data suggest South American surface temperatures remained relatively stable throughout the Holocene across different regions, from the Amazon basin and foothills to the high Andes (e.g., Stute et al., 1995; Punyasena et al., 2008). These results broadly agree with the existing narrative of Holocene temperatures in South America and offer a perspective from the central Andes, showing that high elevation sites experienced a similar magnitude of temperature change as other regions across the continent over the last 20,000 years.

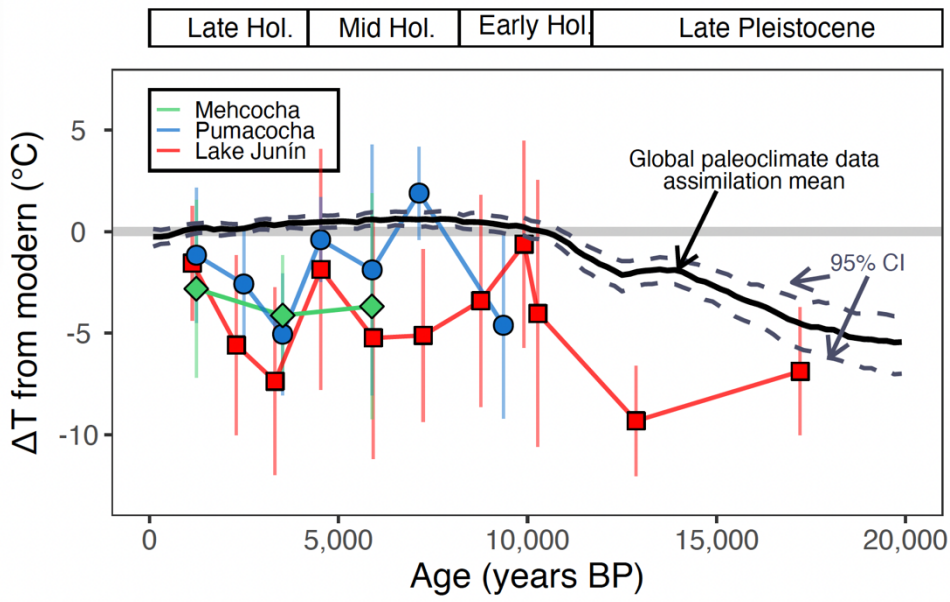

Figure 7: Change in temperature (ΔT) from modern lake water temperatures derived from carbonate $T\Delta_{47}$ values for Lakes Junín, Pumacocha, and Mehcocha (where "modern" is defined as 13 °C, Katz et al., 2023). Also shown is a global paleoclimate data assimilation mean (black; and 95% CI, grey dashed line) plotted as the difference from global mean surface temperature (Osman et al., 2021).

7.3.2. *Holocene P–E in the central Andes*

In Section 7.2.3, we establish that hydrologic variations at the three study lakes correspond with Holocene *P–E* changes in the Lake Junín region. To explore whether these variations reflect local conditions or are broadly representative of regional conditions in the central Andes, we compare our data to other proxy and modeling studies from the central Andes.

Robust evidence of Holocene *P–E* variations in the central Andes are also recorded by lake level data from Lake Junín (Weidhaas, 2017; Woods, 2021) and changes in clastic sediment flux at glacial lake Yanacocha (Stansell et al., 2015) (Figure 8). Lake level records from Lake Junín were derived by correlating changes in sedimentology and shallow water unconformities across a series of sediment cores collected in a lateral transect from shallow to deep waters and provides a useful point of comparison to our isotope data (Figure 8a) (Weidhaas, 2017; Woods, 2021). Reconstructed Lake Junín water level data for the last 25,000 years indicate lake level was high and similar (within 2 m) to present during the late Pleistocene until dropping rapidly (by 4 m) at 13,700 years BP, just before the start of the Holocene. After rising briefly by ~2.5 m at 13,100 years BP, a second precipitous drop occurred in the early Holocene with lake level reaching its lowest point at ~7.5 m below modern water level around 9,700 years BP. Following this minimum, lake level increased steadily over the mid-Holocene (8,200 to 4,200 years BP), reaching near-modern levels at the start of the late Holocene and remained relatively high (within 2.5 m of modern) until present (Figure 8a) (Weidhaas, 2017; Woods, 2021). Records of clastic sediment flux at Yanacocha (10.56 °S, 75.93 °W), located 50 km northeast of Lake Junín also record local hydrology, as higher clastic inputs reflect a relatively advanced position of the Huagurucho glacier, whereby glacier advance is closely related to positive local water balance (Figure 8b) (Sagredo et al., 2014; Stansell et al., 2015). Similar to the other hydrologic proxies, clastic flux values indicate wet conditions in the late Pleistocene (until around 12,000 years BP), followed by overall dry conditions through the early and mid-Holocene (11,700 to 4,200 years BP), before the return of wetter conditions in the late Holocene (after 4,200 years BP).

Hydroclimate variability in the Holocene has also been approached with model data from CMIP6 (Hancock et al. 2023). CMIP6 model results suggest that annual precipitation amount in the central Andes and core monsoon region was lower at 6,000 years BP (i.e., their "mid-Holocene" time-slice) compared to the pre-Industrial (500 years BP), while the opposite trend is observed in the northern hemisphere. The decrease in annual precipitation reflects large reductions in precipitation during the austral summer, corresponding to weakened SASM during the mid-Holocene (Hancock et al., 2023). These results suggest that reduced summer precipitation may contribute substantially to the *P–E* changes in the central Andes. Conversely, as northern hemisphere monsoons weakened over the Holocene, water balance became more negative (e.g., Haug et al., 2001; Metcalfe et al., 2015; Cheng et al., 2023). The stable lake water temperatures in the Lake Junín region (Figure 5c) suggest the influence of temperature on evaporation rates may have been relatively stable over the Holocene. However, calculating quantitative evaporation rates is not possible with our data because, in addition to temperature, evaporation is highly sensitive to changes in other factors that we cannot reliably constrain for these lakes in the Holocene, such as radiation, cloud cover, wind speed, and humidity (e.g., Penman, 1948).

When considering the hydrologic records from the central Andes alongside modeling results, we find it likely that during the early and mid-Holocene (11,700 to 4,200 years BP), hydrologic conditions were drier than present (as reflected by high X_E values among local lakes, low lake levels at Junín, and reduced input of glacial sediment; Figure 8) and characterized by diminished summer precipitation and low *P–E*. Interestingly, while the lake levels and lake carbonate $\delta^{18}O$ records closely track southern hemisphere summer insolation changes, the driest conditions recorded by $\Delta'^{17}O_{rlw}$ values slightly lag the southern hemisphere's insolation minimum (Figure 5a,e). This could suggest that either *P–E* changes in the central Andes were delayed compared to the timing of external climate forcings (i.e., orbital factors), or that additional drivers also contributed to *P–E* changes during the Holocene (or some combination of the two). These observations highlight the need for additional well-dated and high-resolution *P–E* records throughout the central Andes which can complement records of SASM variations. Despite the slight temporal offsets, these data suggest that the water balance history of the central Andes reflects a coherent, regional story of water stressed conditions in the early and mid-Holocene (11,700 to 4,200 years BP), followed by wetter, modern hydrologic conditions in the late Holocene (4,200 years BP to present).

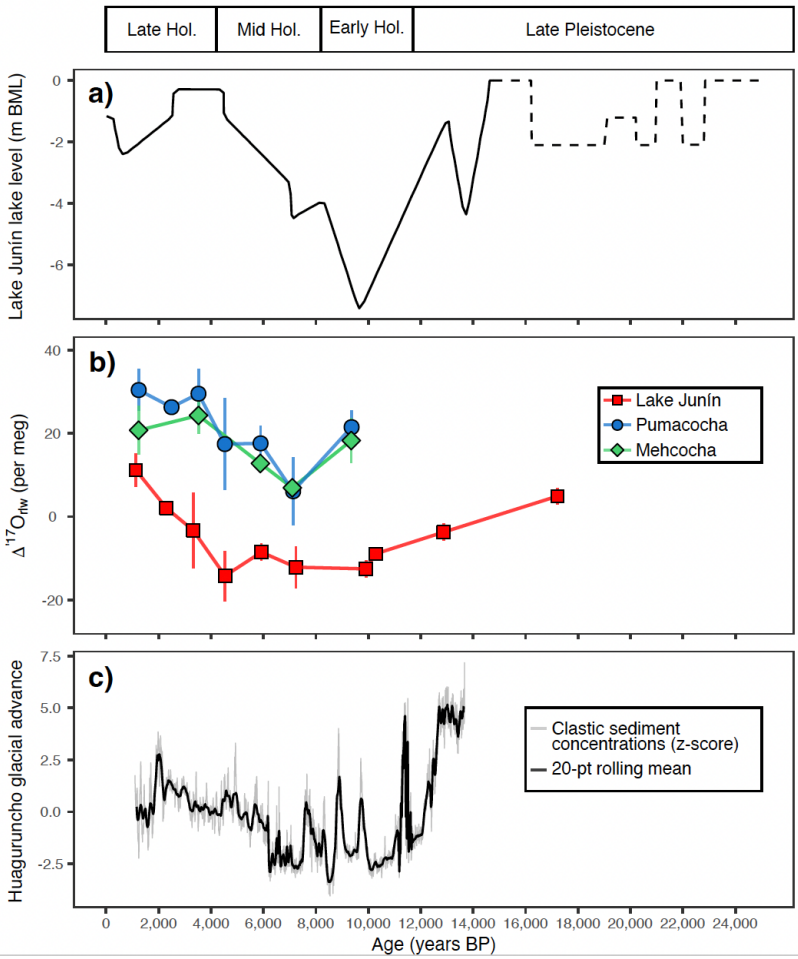

Figure 8: Regional hydroclimate records. (a) Lake Junín lake level shown as meters below modern lake level (m BML) (Weidhaas, 2017; Woods, 2021). (b) Reconstructed lake water $\Delta'^{17}O$ ($\Delta'^{17}O_{rlw}$) values for Lake Junín, Pumacocha, and Mehcocha, as in Figure 5e. (c) Clastic sediment concentrations from Lake Yanacocha shown as the first principal component of sediment geochemical data, where the first principal component corresponds with

843 glacial flour (z-score; grey line) and a 20-point rolling mean (black line) (Stansell et al., 2015); higher values reflect
844 a more advanced position of the Huaguruncho glacier and positive regional water balance.
845
846 **8. Conclusions:**
847 In this study, we present a framework for using clumped and triple oxygen isotopes of
848 lacustrine carbonates to investigate regional temperature and evaporative histories, and to
849 constrain the influence of these factors on lake carbonate $\delta^{18}O$ records. We apply this framework
850 to three lakes in the Peruvian Andes: Lakes Junín, Pumacocha, and Mehcocha. Water temperatures
851 derived from carbonate clumped isotopes were indistinguishable from the present day at all three
852 lakes through the Holocene, suggesting little change in environmental temperatures over the last
853 11,700 years. Stable temperatures indicate that temperature change was not a factor driving
854 carbonate $\delta^{18}O$ variations at any of the three lakes during the Holocene. Water temperatures during
855 the latest Pleistocene were ~5 °C lower than they were during the Holocene and today. Based on
856 triple oxygen isotope data, we find that each lake experienced changes in hydrology (i.e., X_E)
857 associated with more evaporated conditions throughout the early and mid-Holocene (11,700 to
858 4,200 years BP). These hydrologic changes co-occurred with weakened SASM strength and dry
859 conditions throughout the central Andes. During the late Holocene, all three lakes became more
860 open, reflecting a positive shift in water balance and wetter conditions. These results confirm that
861 Lake Junín is highly sensitive to regional water balance changes during the Holocene and offer
862 new evidence that Pumacocha and Mehcocha also experienced evaporated conditions through the
863 early and mid-Holocene. This would have led to a positive shift in lake water $\delta^{18}O$ values at Lake
864 Junín compared to precipitation, consistent with previous interpretations of Lake Junín's carbonate
865 $\delta^{18}O$ record. Changes in water balance at these lakes are concurrent with lake level changes and
866 glacial advance from the central Peruvian Andes, suggesting a coherency among regional
867 hydroclimate records. Importantly, we find that hydroclimate change throughout the Holocene is
868 closely linked to summer insolation and SASM dynamics, highlighting the clear connections
869 between Andean water balance and global climate, and how these connections can be illuminated
870 from lake carbonate $\Delta'^{17}O$ and Δ_{47} records.
871
872 **Open Research:**
873 All new data are provided within the tables of the main text and the supporting materials. All
874 supplemental tables are also deposited on the University of Michigan Deep Blue repository (Katz
875 et al., 2024a). Clumped and triple oxygen isotope data (replicate level data for all samples and
876 standards) are available on the Earth Chem repository (Katz et al., 2024b). Oxygen, carbon, and
877 radiocarbon isotope data, core age models, and summarized clumped and triple oxygen isotope
878 data are available in the on the NOAA National Centers for Environmental Information repository
879 (Katz et al., 2024c). Supplementary code is available within the supporting materials (Text S3)
880 and on Zenodo (Katz, 2024).
881
882 **Acknowledgements**:
883 We thank Kirsten Andrews, Matthew Salinas, Million Mengesha, Julia Kelson, Natalie Packard,
884 Tyler Huth, Nick Ellis, Nick Weidhaas, and Kristina Brady Shannon for analytical and field
885 assistance. We also thank David Gillikin, Elizabeth Olson, Larry Edwards, Dylan Parmenter,
886 Jungpyo Hong, Laura Lopera, Josef Werne, Pedro Tapia, members of the Isotopologue
887 Paleosciences Lab, and members of UM Paleoclimate seminar for useful discussions that improved
888 the presentation of this work. We thank two anonymous reviewers and Editor Matthew Huber for

their constructive comments. We acknowledge the late Herb Wright and Geoff Seltzer for their early work on Lake Junín which was foundational to this study. The authors declare no conflicts of interest.

Funding was provided by: The Geologic Society of America Graduate Student Research Grant (SAK), Scott Turner Award (SAK), Rackham Predoctoral Fellowship (SAK), NSF EAR-2102843 (NEL, BHP), NSF EAR-2102996 (DTR), NSF EAR-2103082 (MBA) and the UM Department of Earth & Environmental Sciences (NEL, BHP, SAK).

CRediT statement:

Conceptualization: SAK, NEL, MBA, DTR, BHP, NMD.
Validation: SAK.
Formal analysis: SAK, NEL, MBA, AW.
Investigation: SAK, NEL, MBA, DJL, AW.
Resources: NEL, MBA, DTR, BHP.
Data Curation: SAK, NEL, MBA, DTR, BHP, DJL, AW.
Writing – Original Draft: SAK, NEL.
Writing – Review & Editing: SAK, NEL, MBA, DTR, BHP, NMD, DJL, AW.
Visualization: SAK.
Supervision: NEL, MBA, DTR.
Project administration: SAK, NEL, MBA, DTR.
Funding acquisition: SAK, NEL, MBA, DTR, BHP.

References:

Abbott, M.B., Binford, M.W., Brenner, M., and Kelts, K.R., 1997, A 3500 ^{14}C yr High-Resolution Record of Water-Level Changes in Lake Titicaca, Bolivia/Peru: Quaternary Research, v. 47, p. 169–180, doi:10.1006/qres.1997.1881.

Aggarwal, P.K., Romatschke, U., Araguas-Araguas, L., Belachew, D., Longstaffe, F.J., Berg, P., Schumacher, C., and Funk, A., 2016, Proportions of convective and stratiform precipitation revealed in water isotope ratios: Nature Geoscience, v. 9, p. 624–629, doi:10.1038/ngeo2739.

Anderson, N.T. et al., 2021, A Unified Clumped Isotope Thermometer Calibration (0.5–1,100°C) Using Carbonate-Based Standardization: Geophysical Research Letters, v. 48, doi:10.1029/2020GL092069.

Aron, P.G., Levin, N.E., Beverly, E.J., Huth, T.E., Passey, B.H., Pelletier, E.M., Poulsen, C.J., Winkelstern, I.Z., and Yarian, D.A., 2021a, Triple oxygen isotopes in the water cycle: Chemical Geology, v. 565, p. 1–23, doi:10.1016/j.chemgeo.2020.120026.

Aron, P.G., Li, S., Brooks, J.R., Welker, J.M., and Levin, N.E., 2023, Seasonal Variations in Triple Oxygen Isotope Ratios of Precipitation in the Western and Central United States: Paleoceanography and Paleoclimatology, v. 38, doi:10.1029/2022PA004458.

Aron, P.G., Poulsen, C.J., Fiorella, R.P., Levin, N.E., Acosta, R.P., Yanites, B.J., and Cassel, E.J., 2021b, Variability and Controls on $\delta^{18}O$, d-excess, and $\Delta'^{17}O$ in Southern Peruvian Precipitation: Journal of Geophysical Research: Atmospheres, v. 126, p. 1–18, doi:10.1029/2020JD034009.

Assonov, S., Groening, M., Fajgelj, A., Hélie, J., and Hillaire-Marcel, C., 2020, Preparation and characterisation of IAEA-603, a new primary reference material aimed at the VPDB scale realisation for $\delta^{13}C$ and $\delta^{18}O$ determination: Rapid Communications in Mass Spectrometry, v. 34, doi:10.1002/rcm.8867.

Barkan, E., and Luz, B., 2007, Diffusivity fractionations of $H_2{}^{16}O/H_2{}^{17}O$ and $H_2{}^{16}O/H_2{}^{18}O$ in air and their implications for isotope hydrology: Rapid Communications in Mass Spectrometry, v. 21, p. 2999–3005, doi:10.1002/rcm.3180.

Benson, L. V, and White, J.W.C., 1994, Stable Isotopes of Oxygen and Hydrogen in the Truckee River Pyramid Lake Surface-Water System .1. Data-Analysis and Extraction of Paleoclimatic Information: Limnology and Oceanography, v. 39, p. 344–355.

Bernasconi, S.M., Müller, I.A., Bergmann, K.D., Breitenbach, S.F.M., Fernandez, A., Hodell, D.A., Jaggi, M., Meckler, A.N., Millan, I., and Ziegler, M., 2018, Reducing Uncertainties in Carbonate Clumped Isotope Analysis Through Consistent Carbonate-Based Standardization: Geochemistry, Geophysics, Geosystems, v. 19, p. 2895–2914, doi:10.1029/2017GC007385.

Bird, B.W., Abbott, M.B., Rodbell, D.T., and Vuille, M., 2011a, Holocene tropical South American hydroclimate revealed from a decadally resolved lake sediment $\delta^{18}O$ record: Earth and Planetary Science Letters, v. 310, p. 192–202, doi:10.1016/J.EPSL.2011.08.040.

Bird, B.W., Abbott, M.B., Vuille, M., Rodbell, D.T., Stansell, N.D., and Rosenmeier, M.F., 2011b, A 2,300-year-long annually resolved record of the South American summer monsoon from the Peruvian Andes: Proceedings of the National Academy of Sciences, v. 108, p. 8583–8588, doi:10.1073/pnas.1003719108.

Cheng, Y., Zhang, C., Li, Y., Li, X., Liu, W., and Zhao, C., 2023, Increasing lake evaporation over the Holocene revealed by oxygen stable isotope in Indian-monsoon dominated

southwestern China: Global and Planetary Change, v. 228, p. 104217, doi:10.1016/j.gloplacha.2023.104217.

Cobbing, J., Quispesivana, L.Q., and Paz, M.M., 1996, Geologia de los cuadrangulos de Ambo, Cerro de Pasco y Ondores:, https://hdl.handle.net/20.500.12544/200 (accessed February 2024).

Cohen, K.M., Finney, S.C., Gibbard, P.L., and Fan, J.-X., 2013, The ICS International Chronostratigraphic Chart: Episodes, v. 36, p. 199–204, doi:10.18814/epiiugs/2013/v36i3/002.

Cohen, K.M., Harper, D.A.T., Gibbard, S.C., and Car, N., 2023, International Chronostratigraphic Chart v2023/09: International Commission on Stratigraphy, www.stratigraphy.org (accessed December 2023).

Craig, H., 1961, Isotopic Variations in Meteoric Waters: Science, v. 133, p. 1702–1703.

Criss, R.E., 1999, Principles of Stable Isotope Distribution: New York, Oxford University Press, 1–254 p.

Crucifix, M., 2016, Insolation for Paleoclimate Studies "palinsol" v0.93, https://bitbucket.org/mcrucifix/insol (accessed January 2023).

Cruz, F.W., Burns, S.J., Karmann, I., Sharp, W.D., Vuille, M., Cardoso, A.O., Ferrari, J.A., Silva Dias, P.L., and Viana, O., 2005, Insolation-driven changes in atmospheric circulation over the past 116,000 years in subtropical Brazil: Nature, v. 434, p. 63–66, doi:10.1038/nature03365.

Cruz, F.W., Vuille, M., Burns, S.J., Wang, X., Cheng, H., Werner, M., Lawrence Edwards, R., Karmann, I., Auler, A.S., and Nguyen, H., 2009, Orbitally driven east-west antiphasing of South American precipitation: Nature Geoscience, v. 2, p. 210–214, doi:10.1038/ngeo444.

Daëron, M., Blamart, D., Peral, M., and Affek, H.P., 2016, Absolute isotopic abundance ratios and the accuracy of Δ_{47} measurements: Chemical Geology, v. 442, p. 83–96, doi:10.1016/j.chemgeo.2016.08.014.

Dansgaard, W., 1964, Stable isotopes in precipitation: Tellus, v. 16, p. 436–468, doi:10.3402/tellusa.v16i4.8993.

Dee, S., Emile-Geay, J., Evans, M.N., Allam, A., Steig, E.J., and Thompson, D.M., 2015, PRYSM: An open-source framework for PRoxY System Modeling, with applications to oxygen-isotope systems: Journal of Advances in Modeling Earth Systems, v. 7, p. 1220–1247, doi:10.1002/2015MS000447.

Dee, S.G., Russell, J.M., Morrill, C., Chen, Z., and Neary, A., 2018, PRYSM v2.0: A Proxy System Model for Lacustrine Archives: Paleoceanography and Paleoclimatology, v. 33, p. 1250–1269, doi:10.1029/2018PA003413.

Ellis, N.M., and Passey, B.H., 2023, A novel method for high-precision triple oxygen isotope analysis of diverse Earth materials using high temperature conversion–methanation–fluorination and isotope ratio mass spectrometry: Chemical Geology, doi:10.1016/j.chemgeo.2023.121616.

Fetrow, A.C., Snell, K.E., Di Fiori, R. V., Long, S.P., and Bonde, J.W., 2022, How Hot Is Too Hot? Disentangling Mid-Cretaceous Hothouse Paleoclimate From Diagenesis: Paleoceanography and Paleoclimatology, v. 37, doi:10.1029/2022PA004517.

Flusche, M.A., Seltzer, G., Rodbell, D., Siegel, D., and Samson, S., 2005, Constraining water sources and hydrologic processes from the isotopic analysis of water and dissolved strontium, Lake Junin, Peru: Journal of Hydrology, v. 312, p. 1–13, doi:10.1016/j.jhydrol.2005.02.021.

Garreaud, R.D., Vuille, M., Compagnucci, R., and Marengo, J., 2009, Present-day South American climate: Palaeogeography, Palaeoclimatology, Palaeoecology, v. 281, p. 180–195, doi:10.1016/j.palaeo.2007.10.032.

Gat, J.R., 1996, Oxygen and Hydrogen Isotopes in the Hydrologic Cycle: Annual Review of Earth and Planetary Sciences, v. 24, p. 225–262, doi:10.1146/annurev.earth.24.1.225.

Gázquez, F., Morellón, M., Bauska, T., Herwartz, D., Surma, J., Moreno, A., Staubwasser, M., Valero-Garcés, B., Delgado-Huertas, A., and Hodell, D.A., 2018, Triple oxygen and hydrogen isotopes of gypsum hydration water for quantitative paleo-humidity reconstruction: Earth and Planetary Science Letters, v. 481, p. 177–188, doi:10.1016/j.epsl.2017.10.020.

Gibson, J.J., Birks, S.J., and Yi, Y., 2016, Stable isotope mass balance of lakes: A contemporary perspective: Quaternary Science Reviews, v. 131, p. 316–328, doi:10.1016/j.quascirev.2015.04.013.

Google LLC, 2022, Google Earth version 7.3.6.9345:, https://earth.google.com/web/ (accessed December 2023).

Hancock, C.L., McKay, N.P., Erb, M.P., Kaufman, D.S., Routson, C.R., Ivanovic, R.F., Gregoire, L.J., and Valdes, P., 2023, Global Synthesis of Regional Holocene Hydroclimate Variability Using Proxy and Model Data: Paleoceanography and Paleoclimatology, v. 38, doi:10.1029/2022PA004597.

Hansen, B.C.S., Seltzer, G.O., and Wright, H.E., 1994, Late Quaternary vegetational change in the central Peruvian Andes: Palaeogeography, Palaeoclimatology, Palaeoecology, v. 109, p. 263–285, doi:10.1016/0031-0182(94)90179-1.

Haug, G.H., Hughen, K.A., Sigman, D.M., Peterson, L.C., and Röhl, U., 2001, Southward Migration of the Intertropical Convergence Zone Through the Holocene: Science, v. 293, p. 1304–1308, doi:10.1126/science.1059725.

Herwartz, D., Surma, J., Voigt, C., Assonov, S., and Staubwasser, M., 2017, Triple oxygen isotope systematics of structurally bonded water in gypsum: Geochimica et Cosmochimica Acta, v. 209, p. 254–266, doi:10.1016/j.gca.2017.04.026.

Horton, T.W., Defliese, W.F., Tripati, A.K., and Oze, C., 2016, Evaporation induced ^{18}O and ^{13}C enrichment in lake systems: A global perspective on hydrologic balance effects: Quaternary Science Reviews, v. 131, p. 365–379, doi:10.1016/j.quascirev.2015.06.030.

Hren, M.T., and Sheldon, N.D., 2012, Temporal variations in lake water temperature: Paleoenvironmental implications of lake carbonate $\delta^{18}O$ and temperature records: Earth and Planetary Science Letters, v. 337–338, p. 77–84, doi:10.1016/j.epsl.2012.05.019.

Huntington, K.W., Saylor, J., Quade, J., and Hudson, A.M., 2015, High late Miocene-Pliocene elevation of the Zhada Basin, southwestern Tibetan Plateau, from carbonate clumped isotope thermometry: Bulletin of the Geological Society of America, v. 127, p. 181–199, doi:10.1130/B31000.1.

Huntington, K.W., Wernicke, B.P., and Eiler, J.M., 2010, Influence of climate change and uplift on Colorado Plateau paleotemperatures from carbonate clumped isotope thermometry: Tectonics, v. 29, p. 1–19, doi:10.1029/2009TC002449.

Huth, T.E., Passey, B.H., Cole, J.E., Lachniet, M.S., McGee, D., Denniston, R.F., Truebe, S., and Levin, N.E., 2022, A framework for triple oxygen isotopes in speleothem paleoclimatology: Geochimica et Cosmochimica Acta, v. 319, p. 191–219, doi:10.1016/j.gca.2021.11.002.

Ibarra, D.E., Kukla, T., Methner, K.A., Mulch, A., and Chamberlain, C.P., 2021, Reconstructing Past Elevations From Triple Oxygen Isotopes of Lacustrine Chert: Application to the

Eocene Nevadaplano, Elko Basin, Nevada, United States: Frontiers in Earth Science, v. 9, p. 1–19, doi:10.3389/feart.2021.628868.

Jasechko, S., Gibson, J.J., and Edwards, T.W.D., 2014, Stable isotope mass balance of the Laurentian Great Lakes: Journal of Great Lakes Research, v. 40, p. 336–346, doi:10.1016/j.jglr.2014.02.020.

Kanner, L.C., Burns, S.J., Cheng, H., Edwards, R.L., and Vuille, M., 2013, High-resolution variability of the South American summer monsoon over the last seven millennia: insights from a speleothem record from the central Peruvian Andes: Quaternary Science Reviews, v. 75, p. 1–10, doi:10.1016/j.quascirev.2013.05.008.

Katz, S.A., 2024 sarahakatz/HoloceneD17O: Supplemental code for "Holocene temperature and water stress in the Peruvian Andes: insights from lake carbonate clumped and triple oxygen isotopes," [Software] Version 1.0. Zenodo. https://doi.org/10.5281/zenodo.10869051.

Katz, S.A., Levin, N. E., Abbott, M. B., Rodbell, D. T., Passey, B. H., DeLuca, N. M., Larsen, D. J., Woods, A., 2024a. Data associated with "Holocene temperature and water stress in the Peruvian Andes: insights from lake carbonate clumped and triple oxygen isotopes," [Dataset]. Version 1.0. University of Michigan Deep Blue Data. doi.org/10.7302/ct1w-sm35. Accessed 2024-04-11.

Katz, S.A., Levin, N. E., Abbott, M. B., Rodbell, D. T., Passey, B. H., DeLuca, N. M., Larsen, D. J., Woods, A., 2024b. Holocene temperature and water stress in the Peruvian Andes: insights from lake carbonate clumped and triple oxygen isotopes, [Dataset]. Version 1.0. Interdisciplinary Earth Data Alliance (IEDA). doi.org/10.60520/IEDA/113158. Accessed 2024-04-11.

Katz, S.A., Levin, N. E., Abbott, M. B., Rodbell, D. T., Passey, B. H., DeLuca, N. M., Larsen, D. J., Woods, A., 2024c. Peru Lakes 14C Age Model and Carbonate Stable Isotope (d13C, d18O, D47, and D′17O) Data of the Holocene, [Dataset]. Version 1.0. NOAA National Centers for Environmental Information (NCEI) Paleo Data Repository. doi.org/10.25921/xswa-c211. Accessed 2024-04-16.

Katz, S.A., Levin, N.E., Rodbell, D.T., Gillikin, D.P., Aron, P.G., Passey, B.H., Tapia, P.M., Serrepe, A.R., and Abbott, M.B., 2023, Detecting hydrologic distinctions among Andean lakes using clumped and triple oxygen isotopes: Earth and Planetary Science Letters, v. 602, p. 117927, doi:10.1016/j.epsl.2022.117927.

Kim, S.-T., and O'Neil, J.R., 1997, Equilibrium and nonequilibrium oxygen isotope effects in synthetic carbonates: Geochimica et Cosmochimica Acta, v. 61, p. 3461–3475, doi:10.1016/S0016-7037(97)00169-5.

Konecky, B.L., Noone, D.C., and Cobb, K.M., 2019, The Influence of Competing Hydroclimate Processes on Stable Isotope Ratios in Tropical Rainfall: Geophysical Research Letters, v. 46, p. 1622–1633, doi:10.1029/2018GL080188.

Laskar, J., Robutel, P., Joutel, F., Gastineau, M., Correia, A.C.M., and Levrard, B., 2004, A long-term numerical solution for the insolation quantities of the Earth: Astronomy & Astrophysics, v. 428, p. 261–285, doi:10.1051/0004-6361:20041335.

Leng, M.J., and Marshall, J.D., 2004, Palaeoclimate interpretation of stable isotope data from lake sediment archives: Quaternary Science Reviews, v. 23, p. 811–831, doi:10.1016/J.QUASCIREV.2003.06.012.

Lenters, J.D., and Cook, K.H., 1999, Summertime Precipitation Variability over South America: Role of the Large-Scale Circulation: Monthly Weather Review, v. 127, p. 409–431, doi:10.1175/1520-0493(1999)127<0409:SPVOSA>2.0.CO;2.

1095 Liu, X., and Battisti, D.S., 2015, The influence of orbital forcing of tropical insolation on the
1096 climate and isotopic composition of precipitation in South America: Journal of Climate, v.
1097 28, p. 4841–4862, doi:10.1175/JCLI-D-14-00639.1.
1098 Luz, B., and Barkan, E., 2005, The isotopic ratios $^{17}O/^{16}O$ and $^{18}O/^{16}O$ in molecular oxygen and
1099 their significance in biogeochemistry: Geochimica et Cosmochimica Acta, v. 69, p. 1099–
1100 1110, doi:10.1016/j.gca.2004.09.001.
1101 Luz, B., and Barkan, E., 2010, Variations of $^{17}O/^{16}O$ and $^{18}O/^{16}O$ in meteoric waters: Geochimica
1102 et Cosmochimica Acta, v. 74, p. 6276–6286, doi:10.1016/j.gca.2010.08.016.
1103 Majoube, M., 1971, Fractionnement en oxygène 18 et en deutérium entre l'eau et sa vapeur:
1104 Journal de Chimie Physique, v. 68, p. 1423–1436.
1105 Marengo, J.A. et al., 2012, Recent developments on the South American monsoon system:
1106 International Journal of Climatology, v. 32, p. 1–21, doi:10.1002/joc.2254.
1107 Matsuhisa, Y., Goldsmith, J.R., and Clayton, R.N., 1978, Mechanisms of hydrothermal
1108 crystallization of quartz at 250°C and 15 kbar: Geochimica et Cosmochimica Acta, v. 42, p.
1109 173–182, doi:10.1016/0016-7037(78)90130-8.
1110 McGee, D., Donohoe, A., Marshall, J., and Ferreira, D., 2014, Changes in ITCZ location and
1111 cross-equatorial heat transport at the Last Glacial Maximum, Heinrich Stadial 1, and the
1112 mid-Holocene: Earth and Planetary Science Letters, v. 390, p. 69–79,
1113 doi:10.1016/j.epsl.2013.12.043.
1114 Merlivat, L., 1978, Molecular diffusitivies or $H_2{}^{16}O$, $HD^{16}O$, and $H_2{}^{18}O$ in gases: The Journal of
1115 Chemical Physics, v. 69, doi:10.1063/1.436884.
1116 Metcalfe, S.E., Barron, J.A., and Davies, S.J., 2015, The Holocene history of the North
1117 American Monsoon: 'known knowns' and 'known unknowns' in understanding its spatial
1118 and temporal complexity: Quaternary Science Reviews, v. 120, p. 1–27,
1119 doi:10.1016/j.quascirev.2015.04.004.
1120 Ministerio de Energia y Minas, 1979a, Mapa Geologico del Cuadrangulo de Cerro de Pasco: v.
1121 Hoja 22-K.
1122 Ministerio de Energia y Minas, 1979b, Mapa Geologico del Cuadrangulo de Ondores: v. Hoja
1123 23-K.
1124 Ministerio de Energia y Minas, 1979c, Mapa Geologico del Cuadrangulo Ulcumajo: v. Hoja 21-
1125 I.
1126 Osman, M.B., Tierney, J.E., Zhu, J., Tardif, R., Hakim, G.J., King, J., and Poulsen, C.J., 2021,
1127 Globally resolved surface temperatures since the Last Glacial Maximum: Nature, v. 599, p.
1128 239–244, doi:10.1038/s41586-021-03984-4.
1129 Palacios, D. et al., 2020, The deglaciation of the Americas during the Last Glacial Termination:
1130 Earth-Science Reviews, v. 203, p. 103113, doi:10.1016/j.earscirev.2020.103113.
1131 Passey, B.H., Hu, H., Ji, H., Montanari, S., Li, S., Henkes, G.A., and Levin, N.E., 2014, Triple
1132 oxygen isotopes in biogenic and sedimentary carbonates: Geochimica et Cosmochimica
1133 Acta, v. 141, p. 1–25, doi:10.1016/j.gca.2014.06.006.
1134 Passey, B.H., and Ji, H., 2019, On the use of triple oxygen isotopes in lake waters and carbonates
1135 for reconstructing $\delta^{18}O$ of unevaporated precipitation: a case study from the Western United
1136 States: Earth and Planetary Science Letters, v. 518, p. 1–12, doi:10.1016/j.epsl.2019.04.026.
1137 Passey, B.H., Levin, N.E., Cerling, T.E., Brown, F.H., and Eiler, J.M., 2010, High-temperature
1138 environments of human evolution in East Africa based on bond ordering in paleosol
1139 carbonates: Proceedings of the National Academy of Sciences, v. 107, p. 11245–11249,
1140 doi:10.1073/pnas.1001824107.

Penman, H.L., 1948, Natural evaporation from open water, bare soil and grass: Proceedings of the Royal Society of London. Series A. Mathematical and Physical Sciences, v. 193, p. 120–145, doi:10.1098/rspa.1948.0037.

Petersen, S.V. V. et al., 2019, Effects of Improved ^{17}O Correction on Inter-Laboratory Agreement in Clumped Isotope Calibrations, Estimates of Mineral-Specific Offsets, and Temperature Dependence of Acid Digestion Fractionation: Geochemistry, Geophysics, Geosystems, v. 20, p. 3495–3519, doi:10.1029/2018GC008127.

Placzek, C., Quade, J., and Patchett, P.J., 2006, Geochronology and stratigraphy of late Pleistocene lake cycles on the southern Bolivian Altiplano: Implications for causes of tropical climate change: Bulletin of the Geological Society of America, v. 118, p. 515–532, doi:10.1130/B25770.1.

Punyasena, S.W., Mayle, F.E., and McElwain, J.C., 2008, Quantitative estimates of glacial and Holocene temperature and precipitation change in lowland Amazonian Bolivia: Geology, v. 36, p. 667–670, doi:10.1130/G24784A.1.

Rademaker, K., Hodgins, G., Moore, K., Zarrillo, S., Miller, C., Bromley, G.R.M., Leach, P., Reid, D.A., Álvarez, W.Y., and Sandweiss, D.H., 2014, Paleoindian settlement of the high-altitude Peruvian Andes: Science, v. 346, p. 466–469, doi:10.1126/science.1258260.

Riris, P., and Arroyo-Kalin, M., 2019, Widespread population decline in South America correlates with mid-Holocene climate change: Scientific Reports, v. 9, doi:10.1038/s41598-019-43086-w.

Rodbell, D.T. et al., 2022, 700,000 years of tropical Andean glaciation: Nature, v. 607, p. 301–306, doi:10.1038/s41586-022-04873-0.

Rodbell, D.T., Seltzer, G.O., Mark, B.G., Smith, J.A., and Abbott, M.B., 2008, Clastic sediment flux to tropical Andean lakes: records of glaciation and soil erosion: Quaternary Science Reviews, v. 27, p. 1612–1626, doi:10.1016/j.quascirev.2008.06.004.

Rodbell, D.T., Smith, J.A., and Mark, B.G., 2009, Glaciation in the Andes during the Lateglacial and Holocene: Quaternary Science Reviews, v. 28, p. 2165–2212, doi:10.1016/j.quascirev.2009.03.012.

Rozanski, K., Araguás-Araguás, L., and Gonfiantini, R., 1993, Isotopic Patterns in Modern Global Precipitation, *in* Swart, P.K., Lohmann, K.C., McKenzie, J.M., and Savin, S. eds., Climate Change in Continental Isotopic Records Geophysical Monograph, Geophysical Monograph Series, v. 78, p. 1–36, doi:10.1029/GM078p0001.

Rozas-Davila, A., Rodbell, D.T., and Bush, M.B., 2023, Pleistocene megafaunal extinction in the grasslands of Junín-Peru: Journal of Biogeography, v. 50, p. 755–766, doi:10.1111/jbi.14566.

Sagredo, E.A., Rupper, S., and Lowell, T. V., 2014, Sensitivities of the equilibrium line altitude to temperature and precipitation changes along the Andes: Quaternary Research, v. 81, p. 355–366, doi:10.1016/j.yqres.2014.01.008.

Santi, L.M., Arnold, A.J., Ibarra, D.E., Whicker, C.A., Mering, J.A., Lomarda, R.B., Lora, J.M., and Tripati, A., 2020, Clumped isotope constraints on changes in latest Pleistocene hydroclimate in the northwestern Great Basin: Lake Surprise, California: GSA Bulletin, v. 132, p. 2669–2683, doi:10.1130/B35484.1.

Schauble, E.A., Ghosh, P., and Eiler, J.M., 2006, Preferential formation of ^{13}C–^{18}O bonds in carbonate minerals, estimated using first-principles lattice dynamics: Geochimica et Cosmochimica Acta, v. 70, p. 2510–2529, doi:10.1016/j.gca.2006.02.011.

Schiferl, J. et al., 2023, A neotropical perspective on the uniqueness of the Holocene among interglacials: Nature Communications, v. 14, p. 7404, doi:10.1038/s41467-023-43231-0.

Schoenemann, S.W., Schauer, A.J., and Steig, E.J., 2013, Measurement of SLAP2 and GISP $\delta^{17}O$ and proposed VSMOW-SLAP normalization for $\delta^{17}O$ and $^{17}O_{excess}$: Rapid Communications in Mass Spectrometry, v. 27, p. 582–590, doi:10.1002/rcm.6486.

Seltzer, G., Rodbell, D., and Burns, S., 2000, Isotopic evidence for late Quaternary climatic change in tropical South America: Geology, v. 28, p. 35, doi:10.1130/0091-7613(2000)28<35:IEFLQC>2.0.CO;2.

SENAMHI, 2023, Datos Hidrometeorológicos a nivel nacional:, https://www.senamhi.gob.pe/?&p=estaciones (accessed January 2023).

Smith, J.A., Seltzer, G.O., Farber, D.L., Rodbell, D.T., and Finkel, R.C., 2005, Early Local Last Glacial Maximum in the Tropical Andes: Science, v. 308, p. 678–681, doi:10.1126/science.1107075 ARTICLE.

de Souza, J.G. et al., 2019, Climate change and cultural resilience in late pre-Columbian Amazonia: Nature Ecology and Evolution, v. 3, p. 1007–1017, doi:10.1038/s41559-019-0924-0.

Stansell, N.D., Licciardi, J.M., Rodbell, D.T., and Mark, B.G., 2017, Tropical ocean-atmospheric forcing of Late Glacial and Holocene glacier fluctuations in the Cordillera Blanca, Peru: Geophysical Research Letters, v. 44, p. 4176–4185, doi:10.1002/2016GL072408.

Stansell, N.D., Rodbell, D.T., Abbott, M.B., and Mark, B.G., 2013, Proglacial lake sediment records of Holocene climate change in the western Cordillera of Peru: Quaternary Science Reviews, v. 70, p. 1–14, doi:10.1016/J.QUASCIREV.2013.03.003.

Stansell, N.D., Rodbell, D.T., Licciardi, J.M., Sedlak, C.M., Schweinsberg, A.D., Huss, E.G., Delgado, G.M., Zimmerman, S.H., and Finkel, R.C., 2015, Late Glacial and Holocene glacier fluctuations at Nevado Huaguruncho in the Eastern Cordillera of the Peruvian Andes: Geology, v. 43, p. 747–750, doi:10.1130/G36735.1.

Stute, M., Forster, M., Frischkorn, H., Serejo, A., Clark, J.F., Schlosser, P., Broecker, W.S., and Bonani, G., 1995, Cooling of Tropical Brazil (5°C) During the Last Glacial Maximum: Science, v. 269, p. 379–383, doi:10.1126/science.269.5222.379.

Terzer-Wassmuth, S., Araguás-Araguás, L.J., Wassenaar, L.I., and Stumpp, C., 2023, Global and local meteoric water lines for $\delta^{17}O/\delta^{18}O$ and the spatiotemporal distribution of $\Delta'^{17}O$ in Earth's precipitation: Scientific Reports, v. 13, p. 19056, doi:10.1038/s41598-023-45920-8.

Thompson, L.G., Mosely-Thompson, E., Davis, M.E., Lin, P.-N., Henderson, K.A., Cole-Dai, J., Bolzan, J.F., and Liu, K. -b., 1995, Late Glacial Stage and Holocene Tropical Ice Core Records from Huascaran, Peru: Science, v. 269, p. 46–50.

Vera, C., Silvestri, G., Liebmann, B., and González, P., 2006, Climate change scenarios for seasonal precipitation in South America from IPCC-AR4 models: Geophysical Research Letters, v. 33, p. L13707, doi:10.1029/2006GL025759.

Voigt, C., Herwartz, D., Dorador, C., and Staubwasser, M., 2021, Triple oxygen isotope systematics of evaporation and mixing processes in a dynamic desert lake system: Hydrology and Earth System Sciences, v. 25, p. 1211–1228, doi:10.5194/hess-25-1211-2021.

Vuille, M., Burns, S.J., Taylor, B.L., Cruz, F.W., Bird, B.W., Abbott, M.B., Kanner, L.C., Cheng, H., and Novello, V.F., 2012, A review of the South American monsoon history as recorded in stable isotopic proxies over the past two millennia: Climate of the Past, v. 8, p. 1309–1321, doi:10.5194/cp-8-1309-2012.

1232 Vuille, M., and Werner, M., 2005, Stable isotopes in precipitation recording South American
1233 summer monsoon and ENSO variability: Observations and model results: Climate
1234 Dynamics, v. 25, p. 401–413, doi:10.1007/s00382-005-0049-9.
1235 Wang, Z., Schauble, E.A., and Eiler, J.M., 2004, Equilibrium thermodynamics of multiply
1236 substituted isotopologues of molecular gases: Geochimica et Cosmochimica Acta, v. 68, p.
1237 4779–4797, doi:10.1016/j.gca.2004.05.039.
1238 Ward, B.M., Wong, C.I., Novello, V.F., McGee, D., Santos, R. V., Silva, L.C.R., Cruz, F.W.,
1239 Wang, X., Edwards, R.L., and Cheng, H., 2019, Reconstruction of Holocene coupling
1240 between the South American Monsoon System and local moisture variability from
1241 speleothem δ18O and 87Sr/86Sr records: Quaternary Science Reviews, v. 210, p. 51–63,
1242 doi:10.1016/j.quascirev.2019.02.019.
1243 Weidhaas, N., 2017, A 25,000-year lake level history of Lake Junin, Peru from stratigraphic and
1244 oxygen isotope studies [MS Thesis]: University of Pittsburgh.
1245 Woods, A., 2021, A sedimentary perspective from Lake Junín on monsoon strength and
1246 glaciation in the tropical Andes over multiple glacial cycles [PhD Thesis]: University of
1247 Pittsburgh.
1248 Woods, A. et al., 2020, Andean drought and glacial retreat tied to Greenland warming during the
1249 last glacial period: Nature Communications, v. 11, p. 5135, doi:10.1038/s41467-020-19000-
1250 8.
1251 Wostbrock, J.A.G., Cano, E.J., and Sharp, Z.D., 2020, An internally consistent triple oxygen
1252 isotope calibration of standards for silicates, carbonates and air relative to VSMOW2 and
1253 SLAP2: Chemical Geology, p. 1–9, doi:10.1016/j.chemgeo.2019.119432.
1254 Wright, H.E., 1983, Late-Pleistocene glaciation and climate around the Junin Plain, central
1255 Peruvian highlands.: Geografiska Annaler, Series A, v. 65 A, p. 35–43,
1256 doi:10.1080/04353676.1983.11880072.
1257 Young, E.D., Galy, A., and Nagahara, H., 2002, Kinetic and equilibrium mass-dependent isotope
1258 fractionation laws in nature and their geochemical and cosmochemical significance:
1259 Geochimica et Cosmochimica Acta, v. 66, p. 1095–1104, doi:10.1016/S0016-
1260 7037(01)00832-8.
1261

Paleoceanography and Paleoclimatology

Supporting Information for

Holocene temperature and water stress in the Peruvian Andes: insights from lake carbonate clumped and triple oxygen isotopes

Sarah A. Katz[1], Naomi E. Levin[1], Mark B. Abbott[2], Donald T. Rodbell[3], Benjamin H. Passey[1], Nicole M. DeLuca[4], Darren J. Larsen[5], Arielle Woods[2]

[1]Department of Earth and Environmental Sciences, 1100 North University Ave, University of Michigan, Ann Arbor, MI, 48109, USA

[2]Department of Geology and Environmental Science, 4107 O'Hara Street, University of Pittsburgh, Pittsburgh, PA, 15260, USA

[3]Geosciences Department, 807 Union Street, Union College, Schenectady, NY, 12308, USA

[4]Department of Earth and Planetary Sciences, Johns Hopkins University, 3400 North Charles Street, Baltimore, MD, 21218, USA

[5]Geology Department, 1600 Campus Road, Occidental College, Los Angeles, CA, 90042, USA

Contents of this file

Additional Supporting Information (Files uploaded separately)

Tables S2, S3, and S5 to S9

Introduction

This supplement contains Text S1–S3, Figures S1–S8, and Tables S1–S9 that support the main text.

Text S1. Radiocarbon analysis and age model generation

Radiocarbon analysis was conducted on terrestrial macrofossils collected from both the Lake Junín and Mehcocha sediment cores. Samples and standards were prepared at the University of Pittsburgh using standard protocols (https://sites.uci.edu/keckams/files/2016/12/aba_protocol.pdf). Samples were dated by accelerator mass spectrometry at the W.M. Keck Carbon Cycle AMS facility at the University of California, Irvine. Uncalibrated radiocarbon ages are reported in Table S1 and S4 for Lake Junín and Mehcocha, respectively.

Calibrated ages were calculated using IntCal13 (Reimer et al., 2013). The R package, *bacon* (Blaauw and Christen, 2011), was used to construct age-depth models for both cores using the following settings: *acc.mean* = 20 yr/cm, *acc.shape* = 1.5, *mem.mean* = 0.7, *mem.strength* = 4. Model outputs are shown in Figures S1 and S3 for Lake Junín and Mehcocha, respectively. Modeled mean, median, and 95% CI intervals are reported every 1 cm in Tables S2 and S5 for Lake Junín and Mehcocha, respectively.

Text S2. Decoupling the influence of evaporation and changing input $\delta'^{18}O$ values on lake water $\delta^{18}O$ values

Changes in lake water evaporation and/or the $\delta'^{18}O$ value of water entering a lake ($\delta'^{18}O_I$) result in changes to lake water $\delta'^{18}O$ values (see the interpretive framework discussed in Section 3.2 for details). To decouple the influence of these two factors on reconstructed lake water $\delta'^{18}O$ ($\delta'^{18}O_{rlw}$) values, a "back projection" method was developed by Passey and Ji (2019) whereby reconstructed lake water $\Delta'^{17}O$ ($\Delta'^{17}O_{rlw}$) values are used to estimate and correct for the influence of lake water evaporation on $\delta'^{18}O_{rlw}$ values, leading to estimates of unevaporated $\delta'^{18}O_I$ values. The relationship between $\delta'^{18}O_I$, $\Delta'^{17}O_{rlw}$ and $\delta'^{18}O_{rlw}$ can be described as (Passey and Ji, 2019, Equation 7):

$$\delta'^{18}O_I = \frac{\Delta'^{17}O_I - \Delta'^{17}O_{rlw} + (\lambda_{lake} - \lambda_{ref}) \times \delta'^{18}O_{rlw}}{(\lambda_{lake} - \lambda_{ref})}$$

where $\Delta'^{17}O_I$ is the $\Delta'^{17}O$ value of unevaporated input water (given in units of ‰), λ_{lake} is the lake water fractionation exponent, and λ_{ref} = 0.528 (see Section 2 for further discussion of λ_{ref} and λ_{lake}).

The values $\Delta'^{17}O_{rlw}$ and $\delta'^{18}O_{rlw}$ can be determined from analytical measurements of carbonates, $\Delta'^{17}O$ values of modern precipitation are used to represent $\Delta'^{17}O_I$ (assuming $\Delta'^{17}O_I$ is conserved through time), and an estimation is made for λ_{lake} (Passey and Ji, 2019; Ibarra et al., 2021; Kelson et al., 2022; Katz et al., 2023). Passey and Ji (2019) showed that λ_{lake} can be estimated from $\Delta'^{17}O_{rlw}$ values under a humidity range of 0.3–0.7 and Katz et al. (2023) extended these estimates to humidity between 0.3–0.9.

Here, we calculate $\delta'^{18}O_I$ values for Lake Junín over the course of the Holocene using the back projection method. We do not present $\delta'^{18}O_I$ values for Lakes Pumacocha or Mehcocha because the relatively small degree of evaporation (i.e., $\Delta'^{17}O_{rlw}$ and $\Delta'^{17}O_I$ values are very similar) results in a high degree of uncertainty in λ_{lake}, and by extension, $\delta'^{18}O_I$ values (see Katz et al., 2023). For Lake Junín, we present $\delta'^{18}O_I$ values determined using three different humidity scenarios for estimating λ_{lake} (low, high and a full range of values), following the approach in Katz et al. (2023) (Figure S7; Table S9). We can further refine these estimates by selecting what we believe is the most likely humidity scenario for each sample. Our selection is based qualitatively on $\Delta'^{17}O_{rlw}$

values, as we assume there is a relationship between $\Delta'^{17}O_{rlw}$ and humidity. We use these new $\delta'^{18}O_l$ values to calculate the magnitude of evaporative influence on $\delta'^{18}O_{rlw}$ values by subtracting $\delta'^{18}O_l$ from $\delta'^{18}O_{rlw}$ (Figure S7d).

The magnitude of lake water evaporation varied over the Holocene and led to lake waters which were ~ +9 ‰ (compared to $\delta'^{18}O_l$) during the early and mid-Holocene, but freshened over the Holocene to ~ +5 ‰ (compared to $\delta'^{18}O_l$) during the late Holocene (Figure S7; Table S9). To a first order, changes in the magnitude of evaporation track changes in SASM. The combination of these data reveal that, over the Holocene, changes in $\delta'^{18}O_l$ and lake water evaporation were responsible for changes in $\delta'^{18}O_{rlw}$ values (Figure S7), with the highest $\delta'^{18}O_l$ values during the early Holocene (~ -12.6 ‰, VSMOW-SLAP) before decreasing through the mid to late Holocene ($\gtrsim$ -16.6 ‰, VSMOW-SLAP). This decrease of ~4 ‰ is similar to the ~3 ‰ change in $\delta'^{18}O_l$ estimated from local speleothem and ice core records (Thompson et al., 1995; Kanner et al., 2013) and supports prior interpretations that $\delta'^{18}O_l$ values at Lake Junín reflect changes in SASM strength over the Holocene.

Text S3. Deterministic lake water isotope mass balance model for R

```
## DETERMINISTIC LAKE WATER ISOTOPE MASS BALANCE MODEL
## "Holocene temperature and water stress in the Peruvian Andes: insights from lake carbonate clumped and triple oxygen isotopes"
## Paleoceanography and Paleoclimatology
## Sarah A. Katz*, Naomi E. Levin, Mark B. Abbott, Donald T. Rodbell, Benjamin H. Passey, Nicole M. DeLuca, Darren J. Larsen, Arielle Woods
## Correspondence: skatzees@umich.edu (SAK)
## Updated: Dec 12, 2023

## INSTALL AND ATTACH PACKAGES
# install.packages("ggplot2")
# install.packages("ggpubr")
# install.packages("rgl")
library(ggplot2)
library(ggpubr)
library(rgl)

## PLOT PATH
plot.path <- "~/Desktop/"            ## user may update plot path

## STEADY STATE ISOTOPE LAKE BALANCE EQUATIONS (SECTIONS 3.1 AND TABLE 2)
## Rw = (aeq*Ri*(adiff(1-h) + h*(1-F)) + aeq*h*Xe*Rv*F) / (Xe + aeq*(1-Xe)*(adiff*(1-h) + h(1-F))
## Open basin lake where evaporated water contributes to atmospheric vapor (Benson and White, 1994; Passey and Ji, 2019, Eq. 6)

## SET UP
## CONSTANTS
  R18smow = 0.0020052   ## Baertschi, 1976; IAEA Reference sheet
```

```
   R17smow = 0.0003799   ## Li et al., 1988; IAEA Reference sheet
   theta.eq = 0.529      ## Barkan and Luz, 2005
   theta.diff = 0.5185   ## Barkan and Luz, 2007
   theta.ref = 0.528
   diffratio18 = 1/0.9723  ## Merlivat, 1978

## USER DEFINED VARIABLES
   temp = 14       ## Lake temperature in degrees Celsius
   Phi = 0.5       ## The relative proportion of diffusive (0; molecular diffusion) to
turbulent (1; non-fractionating) transport of water vapor during evaporation
   h = c(rep(seq(0.1, 0.9, by=0.1), 11))   ## relative humidity at lake surface
   Xe = c(rep(0.0, 9),      ## Volumetric proportion of evaporation (E) to inputs (I).
Xe = E/I. Ranges from open basin lakes (0), to closed basin lake (1.0)
         rep(0.1, 9),
         rep(0.2, 9),
         rep(0.3, 9),
         rep(0.4, 9),
         rep(0.5, 9),
         rep(0.6, 9),
         rep(0.7, 9),
         rep(0.8, 9),
         rep(0.9, 9),
         rep(1.0, 9))

   f = 0.9   ## Fraction of atmospheric vapor derived from distal sources versus
the lake itself
            ## Where 1 and 0 represent exclusively distal and lake-derived sources
of atmospheric vapor, respectively.

   ## INPUT WATER
   ## Based on amount-weighted mean annual precipitation at Junin, Peru (Katz
et al., 2023, EPSL). All in units of per mil.
      D17Oi = 0.031
      dp18Oi = -14.1
      dp17Oi = D17Oi + (dp18Oi * theta.ref)

## Calculate R values for input waters
   Ri18 = exp(dp18Oi/1000)*R18smow
   Ri17 = exp(dp17Oi/1000)*R17smow

## Isotopic ratio of water that atmospheric vapor is in equilibrium with (estimated
from input water values)
   d18Ov = -15     ## water that vapor is in equilibrium with
   D17Ov = 0.035   ## water that vapor is in equilibrium with
```

```
   dp18Ov = log(d18Ov/1000+1)*1000                ## convert vapor d18O to
d'18O
   dp17Ov = D17Ov + theta.ref*dp18Ov              ## calculate vapor d17O to
d'17O

## Temperature dependent equilibrium fractionation factor between vapor and
liquid water
   aeq18 = exp((1137/((temp + 273.15)^2)) - (0.4156/(temp+273.15)) -
0.0020667)    ## Majoube 1971
   aeq17 = exp(theta.eq * log(aeq18))

## Calculate R values for vapor
   Rv18 = (exp(dp18Ov/1000)* R18smow)/aeq18
   Rv17 = (exp(dp17Ov/1000)*R17smow)/aeq17

## Diffusion vs. pure turbulence (i.e. no fractionation). When Phi = 1, 100%
diffusive fractionation; when Phi = 0, 0% diffusive fractionation (all turbulent)
   adiff18 = Phi*diffratio18 + (1-Phi)
   adiff17 = exp(theta.diff*log(adiff18))


## SET UP FOR LOOP
   dat = data.frame(cbind(Xe, h))
   dp18Ow <- vector()          ## Create empty vectors to hold products from for
loop
   d18Ow <- vector()
   dp17Ow <- vector()
   Dp17Ow <- vector()

## OPEN FOR LOOP
   for (i in 1:nrow(dat)){

##  LAKE WATER CALCULATIONS
## Calculate R values for lake waters
# Rw18 = ((aeq18*Ri18*(adiff18*(1-h)+h*(1-f)))+(aeq18*h*Xe*Rv18*f))/
#   (Xe+aeq18*(1-Xe)*(adiff18*(1-h)+h*(1-f)))
#
# Rw17 = ((aeq17*Ri17*(adiff17*(1-h)+h*(1-f)))+(aeq17*h*Xe*Rv17*f))/
#   (Xe+aeq17*(1-Xe)*(adiff17*(1-h)+h*(1-f)))

   Rw18 = ((aeq18*Ri18*(adiff18*(1-dat[i,2])+dat[i,2]*(1-
f)))+(aeq18*dat[i,2]*dat[i,1]*Rv18*f))/
     (dat[i,1]+aeq18*(1-dat[i,1])*(adiff18*(1-dat[i,2])+dat[i,2]*(1-f)))

   Rw17 = ((aeq17*Ri17*(adiff17*(1-dat[i,2])+dat[i,2]*(1-
f)))+(aeq17*dat[i,2]*dat[i,1]*Rv17*f))/
```

```
     (dat[i,1]+aeq17*(1-dat[i,1])*(adiff17*(1-dat[i,2])+dat[i,2]*(1-f)))

## Calculate delta (d) and delta prime (dp) values for lake waters in units of per
mil and D'17O (Dp) in units of per meg.
   dp18Ow. = (log(Rw18/R18smow))*1000
   d18Ow. = ((Rw18/R18smow)-1)*1000
   dp17Ow. = (log(Rw17/R17smow))*1000

   Dp17Ow. = (dp17Ow. - (theta.ref*dp18Ow.))*1000

## Fill empty vectors with newly calculated values
   dp18Ow[i] = dp18Ow.
   d18Ow[i] = d18Ow.
   dp17Ow[i] = dp17Ow.
   Dp17Ow[i] = Dp17Ow.

}

   dat = data.frame(cbind(Xe, h, Phi, f, D17Oi, dp18Oi, temp, dp18Ow, d18Ow,
dp17Ow, Dp17Ow))

   dat

############
## PLOTS ##
############

Xe0 <- subset(dat, dat[,1] == 0)
Xe0.1 <- subset(dat, dat[,1] == 0.1)
Xe0.2 <- subset(dat, dat[,1] == 0.2)
Xe0.3 <- subset(dat, dat[,1] == 0.3)
Xe0.4 <- subset(dat, dat[,1] == 0.4)
Xe0.5 <- subset(dat, dat[,1] == 0.5)
Xe0.6 <- subset(dat, dat[,1] == 0.6)
Xe0.7 <- subset(dat, dat[,1] == 0.7)
Xe0.8 <- subset(dat, dat[,1] == 0.8)
Xe0.9 <- subset(dat, dat[,1] == 0.9)
Xe1 <- subset(dat, dat[,1] == 1)


Fig6 <- ggplot()+
  theme_bw()+
  theme(panel.grid.minor = element_blank(), panel.grid.major =
element_blank())+
  geom_line(aes(x=Xe0$h, y=Xe0$Dp17Ow-Xe0$D17Oi*1000))+
  geom_line(aes(x=Xe0.1$h, y=Xe0.1$Dp17Ow-Xe0$D17Oi*1000))+
```

```
  geom_line(aes(x=Xe0.2$h, y=Xe0.2$Dp17Ow-Xe0$D17Oi*1000))+
  geom_line(aes(x=Xe0.3$h, y=Xe0.3$Dp17Ow-Xe0$D17Oi*1000))+
  geom_line(aes(x=Xe0.4$h, y=Xe0.4$Dp17Ow-Xe0$D17Oi*1000))+
  geom_line(aes(x=Xe0.5$h, y=Xe0.5$Dp17Ow-Xe0$D17Oi*1000))+
  geom_line(aes(x=Xe0.6$h, y=Xe0.6$Dp17Ow-Xe0$D17Oi*1000))+
  geom_line(aes(x=Xe0.7$h, y=Xe0.7$Dp17Ow-Xe0$D17Oi*1000))+
  geom_line(aes(x=Xe0.8$h, y=Xe0.8$Dp17Ow-Xe0$D17Oi*1000))+
  geom_line(aes(x=Xe0.9$h, y=Xe0.9$Dp17Ow-Xe0$D17Oi*1000))+
  geom_line(aes(x=Xe1$h, y=Xe1$Dp17Ow-Xe0$D17Oi*1000))+

  # Late Holocene
  geom_segment(aes(x=-Inf, xend=Inf, y=-8, yend=-8), color="#44cf6c", lwd=1)+
  geom_segment(aes(x=-Inf, xend=Inf, y=-2, yend=-2), color="dodgerblue3",
lwd=1)+
  geom_segment(aes(x=-Inf, xend=Inf, y=-24, yend=-24), color="red", lwd=1)+

  # Early and Mid Holocene
  # geom_segment(aes(x=-Inf, xend=Inf, y=-19, yend=-19), color="#44cf6c",
lwd=1, lty=1)+
  # geom_segment(aes(x=-Inf, xend=Inf, y=-15, yend=-15), color="dodgerblue3",
lwd=1, lty=1)+
  # geom_segment(aes(x=-Inf, xend=Inf, y=-42, yend=-42), color="red", lwd=1,
lty=1)+
  # geom_rect(aes(xmin=0.5, xmax=0.9, ymax=-43+6, ymin=-43-6), fill="red",
alpha=.2)+

  labs(x="Relative humidity", y=expression(Delta*"\u02B9"^"17"*"O"[rlw]*" -
"*Delta*"\u02B9"^"17"*"O"[l]*" (per meg)"), size=5)+
  theme(axis.text=element_text(size=12),axis.title=element_text(size=14),
        panel.background = element_rect(fill='transparent'),plot.background =
element_rect(fill='transparent', color=NA))+
  geom_text(aes(x=0.05, y=subset(dat, dat[,2] == .1)$Dp17Ow-D17Oi*1000),
alpha=1, label=c(seq(0, 1, by=0.1)),  hjust = 0, color="orange")+
  scale_y_continuous(limits = c(-120, 2), expand = c(0, 0), labels =
scales::number_format(accuracy = 1))+
  scale_x_continuous(limits = c(0.05,0.9), n.breaks=8, labels =
scales::number_format(accuracy = .1))

Fig6
# ggsave(filename="Fig6.pdf", plot = Fig6, path=plot.path, device=cairo_pdf,
height=6, width=5 )
```

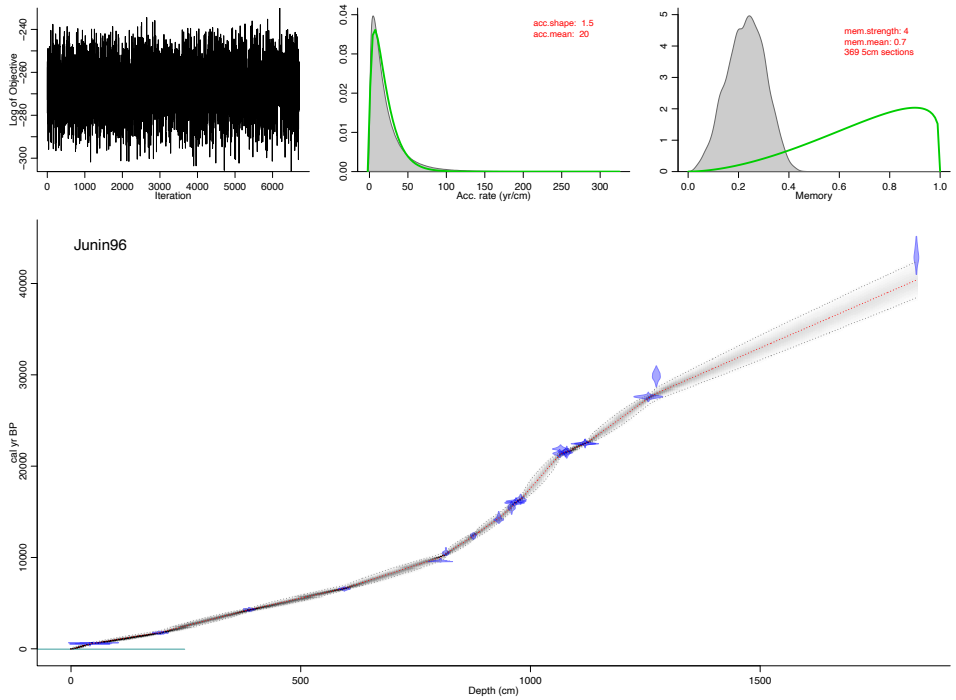

Figure S1. Lake Junín age model produced in the R package *bacon* (Blaauw and Christen, 2011) using the IntCal13 calibration curve of Reimer et al. (2013). ^{14}C radiocarbon dates are provided in Table S1 and model output is provided in Table S2.

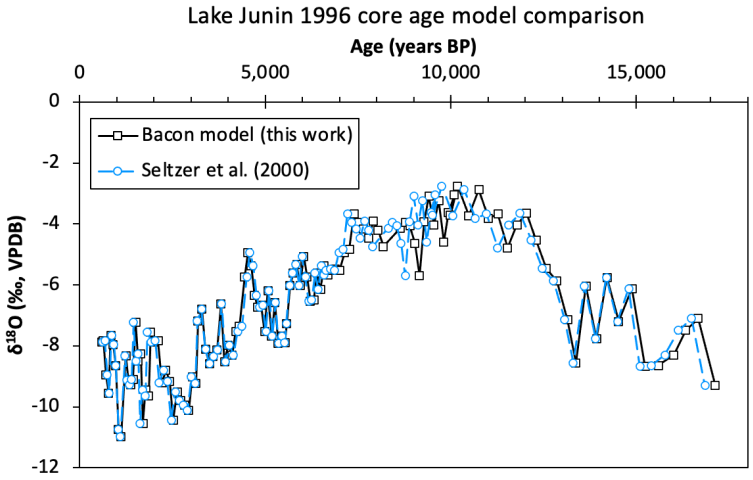

Figure S2. Comparison between the original Lake Junín age model from Seltzer et al. (2000) (dashed blue line, Table S3) and the revised *bacon* age model (solid black line, Figure S1, Table S1–S3).

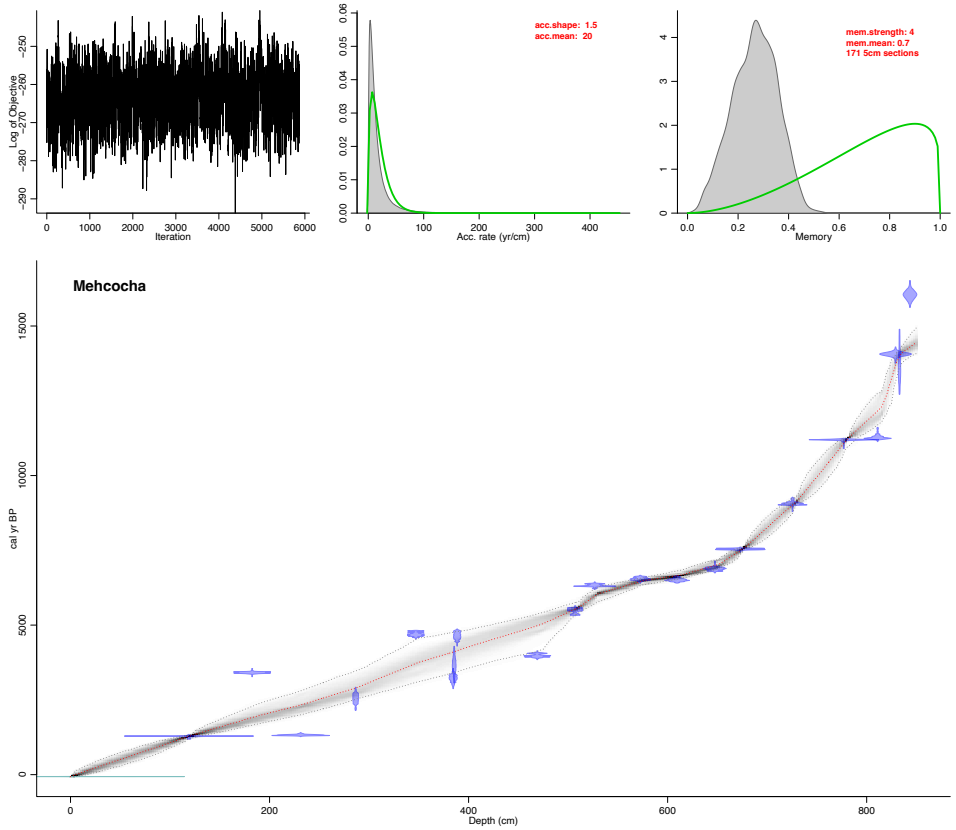

Figure S3. Lake Mehcocha age model produced in the R package *bacon* (Blaauw and Christen, 2013) using the IntCal13 calibration curve of Reimer et al. (2013). ^{14}C radiocarbon dates are provided in Table S4 and model output is provided in Table S5.

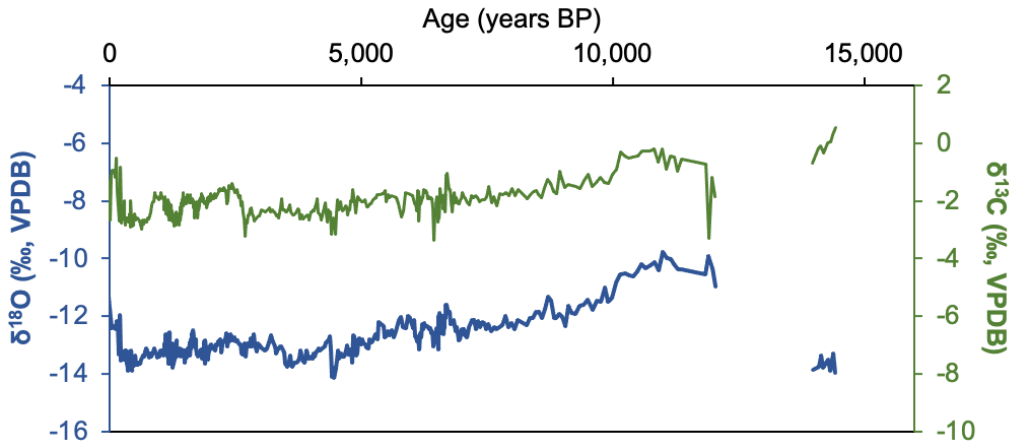

Figure S4. Lake Mehcocha $\delta^{13}C$ and $\delta^{18}O$ records (‰, VPDB). Data are provided in Table S6.

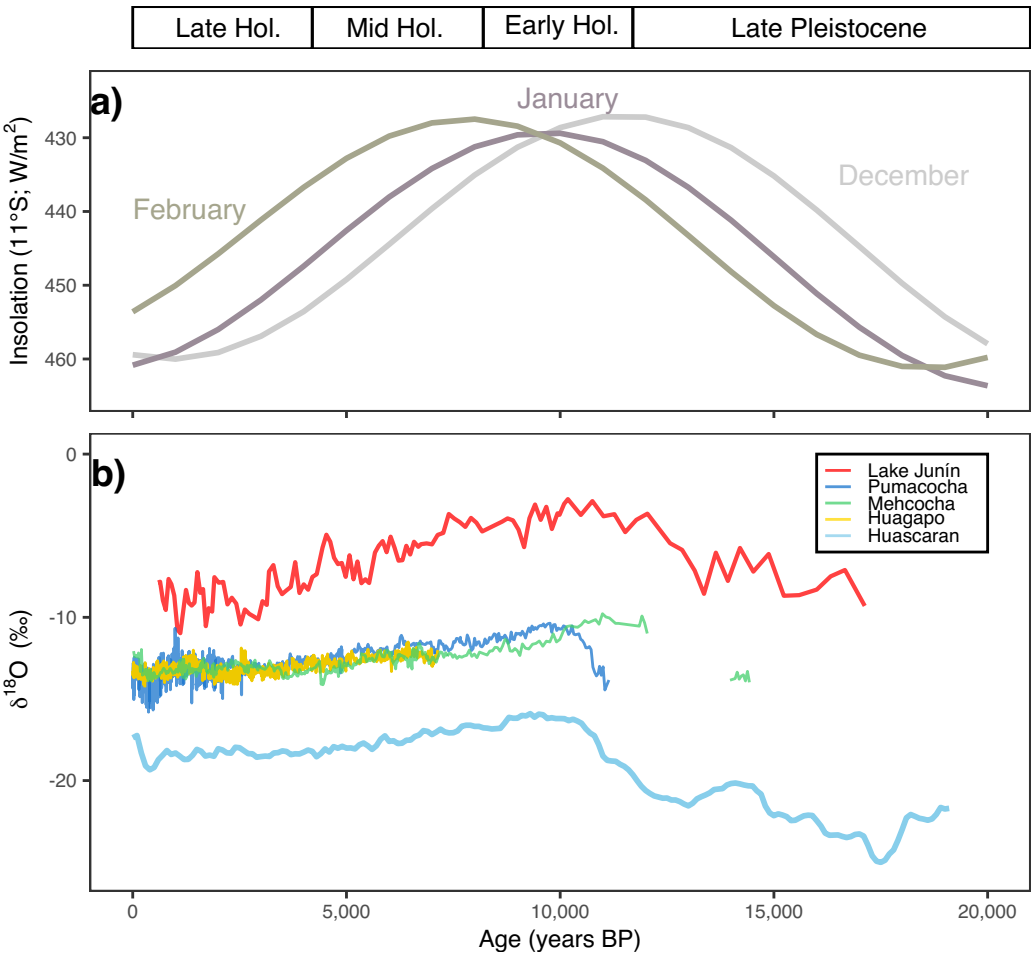

Figure S5. (a) Dec–Feb. insolation at 11 °S, as in Figure 1 (Laskar et al., 2004; Crucifix, 2016). (b) Carbonate $\delta^{18}O$ records from Lakes Junín (Seltzer et al., 2000), Pumacocha (Bird et al., 2011), and Mehcocha (‰, VPDB) shown alongside speleothem $\delta^{18}O$ from Huagapo cave (‰, VPBD) (Kanner et al., 2013) and Huascaran ice core $\delta^{18}O$ (‰,

VSMOW) (Thompson et al., 1995). Lake Junín data is shown on the updated *bacon* age model shown in Figure S1–S2.

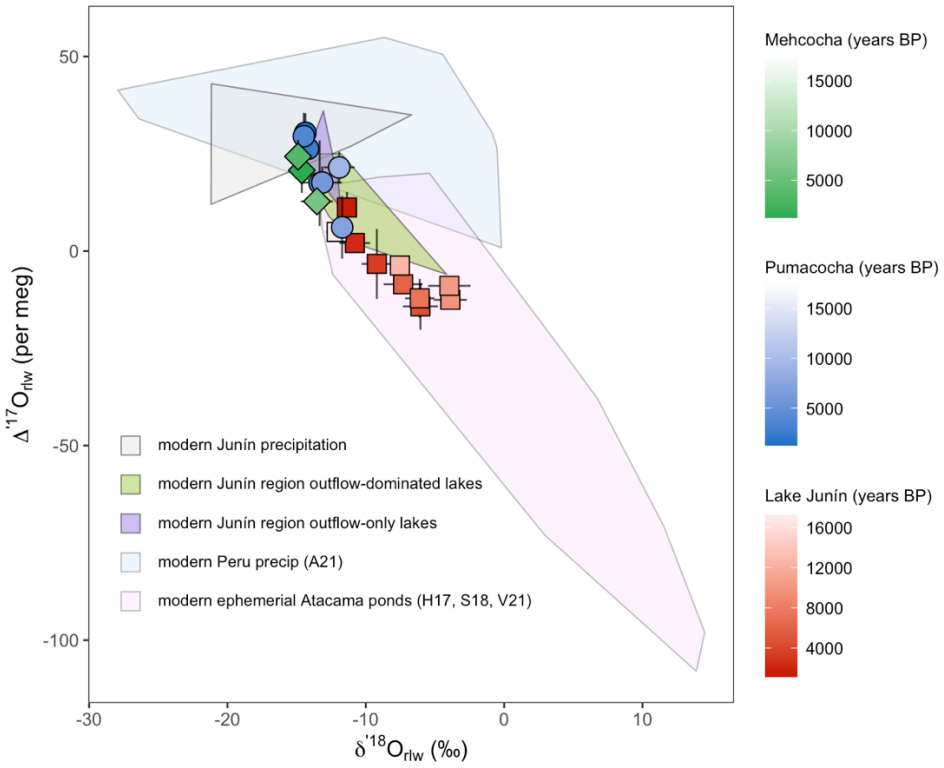

Figure S6. Reconstructed formation water $\Delta'^{17}O$ and $\delta'^{18}O$ values for Lake Junín (red squares), Pumacocha (blue circles), and Mehcocha (green diamonds). See Table 1 for data. Tinted scale bars and symbol fill correspond to sample age. Shaded polygons represent modern water and reconstructed carbonate formation water $\Delta'^{17}O$ and $\delta'^{18}O$ values for Junín precipitation and lakes (Katz et al., 2023). Also shown are polygons representing the range of modern precipitation $\Delta'^{17}O$ and $\delta'^{18}O$ values observed in Peru

(data from Aron et al., 2021) and waters from modern ephemeral ponds in the Atacama (data from Herwartz et al., 2017; Surma et al., 2018; Voigt et al., 2021).

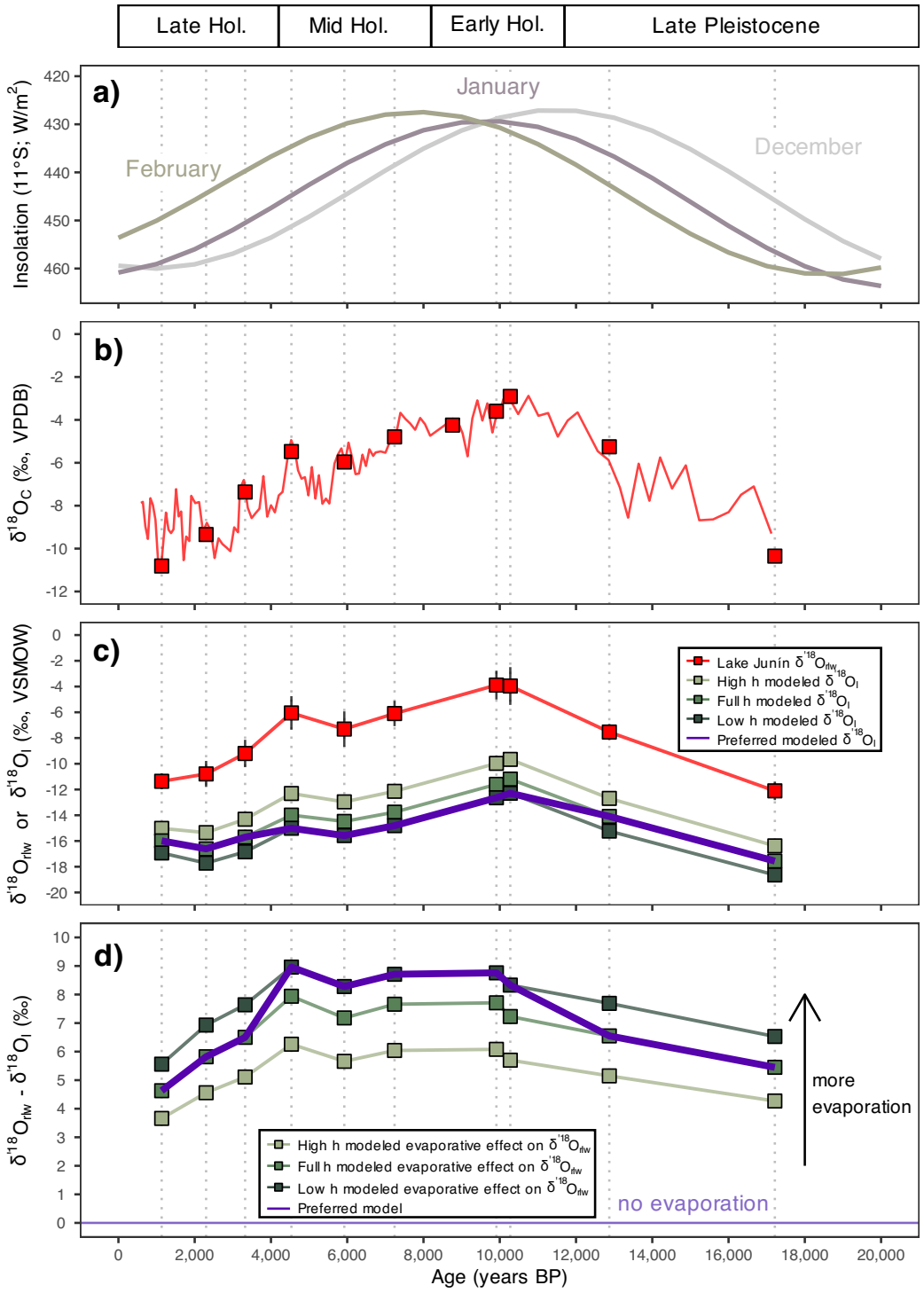

Figure S7. (a) Dec–Feb. insolation at 11 °S, as in Figure 1 (Laskar et al., 2004; Crucifix, 2016). (b) Carbonate $\delta^{18}O$ record from Lake Junín (Seltzer et al., 2000), with $\delta^{18}O$ measurements from Δ_{47} analysis shown as red squares. (c) As in Figure 5, reconstructed

lake water $\delta'^{18}O$ ($\delta'^{18}O_{rlw}$) values derived from carbonate clumped isotope $\delta^{18}O$ and $T\Delta_{47}$ values; error bars represent 2σ SD propagated uncertainty. Also shown is reconstructed input water $\delta'^{18}O$ ($\delta'^{18}O_I$) calculated from $\delta'^{18}O_{rlw}$ and $\Delta'^{17}O_{rlw}$ using the back projection approach of Passey and Ji (2019) using three different humidity scenarios to calculate λ_{lake} (see Katz et al., 2023). (d) The difference between $\delta'^{18}O_{rlw}$ and $\delta'^{18}O_I$ is shown for the three humidity scenarios and represents the magnitude by which $\delta'^{18}O_{rlw}$ values are evaporatively enriched in ^{18}O with respect to $\delta'^{18}O_I$ values. The purple lines in both (c) and (d) show preferred solutions for each sample across the three humidity scenarios; we qualitatively selected the high, full, and low humidity scenarios for $\Delta'^{17}O_{rlw}$ values >20 per meg, -5 to 20 per meg, and <-5 per meg, respectively. See Table S9 for the data plotted in both (c) and (d).

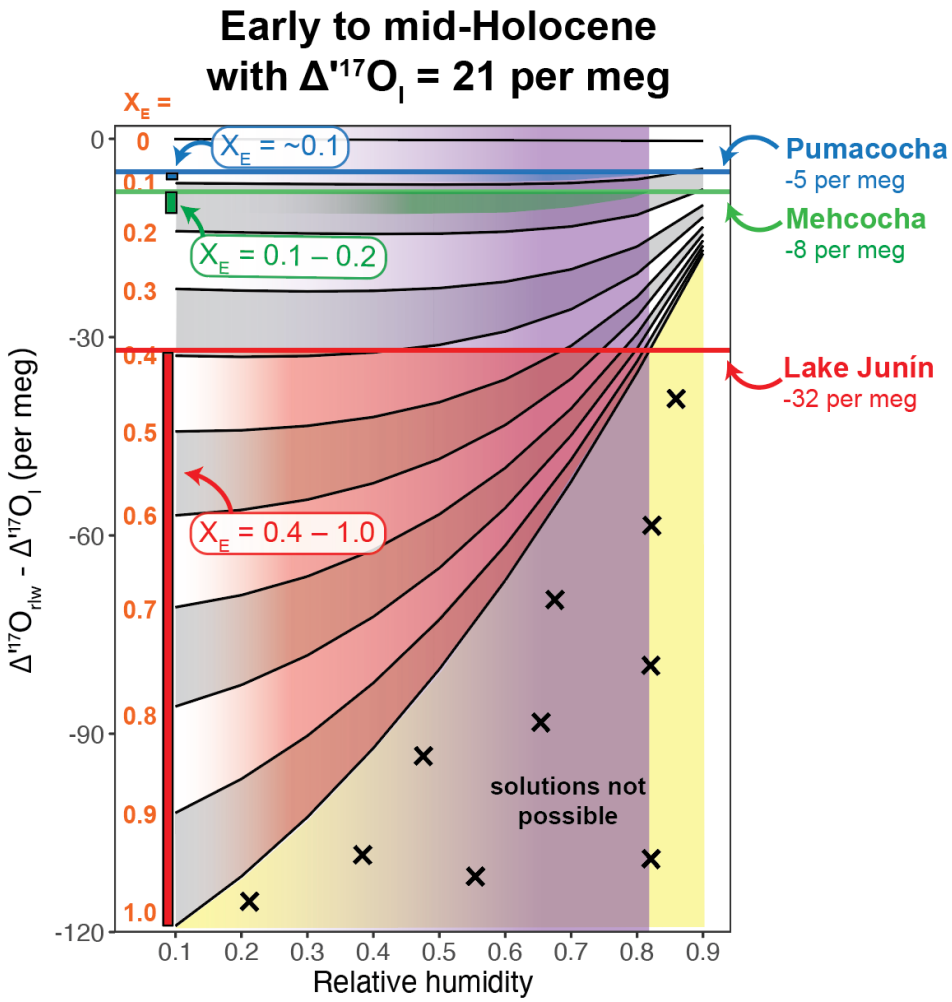

Figure S8. X_E estimates for Lakes Junín, Pumacocha, and Mehcocha during the early and mid-Holocene assuming a different $\Delta'^{17}O_I$ value (21 per meg). Model parameters are the same as in Table 2.

Table S1. Lake Junín radiocarbon age data.

Lab Number	Radiocarbon age (^{14}C yr BP)	Radiocarbon age uncertainty (1 σ)	Composite Depth (cm)
Top-1*	-46	1	0
AA-24001**	520	40	41
OS-16053**	680	30	49
OS-16054**	1820	40	194.5
OS-16055**	3880	45	388
OS-16056**	5760	60	595
OS-16057**	8640	40	804
OS-25946	9320	95	816
OS-25945	10490	95	876
OS-25947	12240	100	931
OS-16052**	12950	150	959
UCIAMS-193108	13285	35	965.5
UCIAMS-193109	13415	40	968.5
AA-24002**	13560	95	978.5
UCIAMS-193110	17670	60	1063.5
UCIAMS-193111	18070	70	1065.5
UCIAMS-193141	17750	60	1076.5
AA-24003**	17795	145	1079
UCIAMS-193142	18605	55	1118.5
CAMS-71936	18620	80	1119
CAMS-71935	23400	150	1256.5
OS-18137**	25700	330	1274
AA-24004**	39020	1045	1840

* Core top age defined as collection year (1996) ± 1 year.

** Published previously by Selzer et al. (2000).

Table S2. Lake Junín bacon age model output.

Table S3. Lake Junín δ^{13}C and δ^{18}O data.

Table S4. Lake Mehcocha radiocarbon age dates.

Lab Number	Radiocarbon age (^{14}C yr BP)	Radiocarbon age uncertainty (1 σ)	Composite Depth (cm)
Top-1*	-65	1	0
172627	1355	15	119
209801	3190	20	182.5
164807	1420	20	231.25
209802	2480	120	286.5
172628	4150	15	347
209803	3040	80	384.5
209796	3390	200	385.5
209804	4120	80	388.5
172629	3655	20	469
164808	4760	45	507
164809	5520	30	526.75
164810	5745	25	572.5
164811	5720	25	609.5
164812	6040	25	647.5
172630	6665	15	673
164813	8120	30	725.5
172631	9750	20	777
164814	9855	45	811
172632	12165	25	829
209797	11680	440	833
164815	13340	80	843.5

* Core top age defined as collection year (2015) ± 1 year.

Table S5. Lake Mehcocha bacon age model output.

Table S6. Mehcocha $\delta^{13}C$ and $\delta^{18}O$ data.

Table S7. Carbonate Δ_{47} data for Lakes Junín, Pumacocha, and Mehcocha.

Table S8. Carbonate $\Delta'^{17}O$ data for Lakes Junín, Pumacocha, and Mehcocha.

Table S9. Lake Junín reconstructed input $\delta'^{18}O$ ($\delta'^{18}O_l$) values

References for Supplementary Information:

Aron, P.G., Poulsen, C.J., Fiorella, R.P., Levin, N.E., Acosta, R.P., Yanites, B.J., and Cassel, E.J., 2021, Variability and Controls on $\delta^{18}O$, d-excess, and $\Delta'^{17}O$ in Southern Peruvian Precipitation: Journal of Geophysical Research: Atmospheres, v. 126, p. 1–18, doi:10.1029/2020JD034009.

Bird, B.W., Abbott, M.B., Rodbell, D.T., and Vuille, M., 2011, Holocene tropical South American hydroclimate revealed from a decadally resolved lake sediment $\delta^{18}O$ record: Earth and Planetary Science Letters, v. 310, p. 192–202, doi:10.1016/J.EPSL.2011.08.040.

Blaauw, M., and Christen, J.A., 2011, Flexible paleoclimate age-depth models using an autoregressive gamma process: Bayesian Analysis, v. 6, p. 457–474, doi:10.1214/11-BA618.

Crucifix, M., 2016, Insolation for Paleoclimate Studies “palinsol” v0.93:, https://bitbucket.org/mcrucifix/insolhttps://bitbucket.org/mcrucifix/insol (accessed January 2023).

Herwartz, D., Surma, J., Voigt, C., Assonov, S., and Staubwasser, M., 2017, Triple oxygen isotope systematics of structurally bonded water in gypsum: Geochimica et Cosmochimica Acta, v. 209, p. 254–266, doi:10.1016/j.gca.2017.04.026.

Ibarra, D.E., Kukla, T., Methner, K.A., Mulch, A., and Chamberlain, C.P., 2021, Reconstructing Past Elevations From Triple Oxygen Isotopes of Lacustrine Chert: Application to the Eocene Nevadaplano, Elko Basin, Nevada, United States: Frontiers in Earth Science, v. 9, p. 1–19, doi:10.3389/feart.2021.628868.

Kanner, L.C., Burns, S.J., Cheng, H., Edwards, R.L., and Vuille, M., 2013, High-resolution variability of the South American summer monsoon over the last seven millennia: insights from a speleothem record from the central Peruvian Andes: Quaternary Science Reviews, v. 75, p. 1–10, doi:10.1016/j.quascirev.2013.05.008.

Katz, S.A., Levin, N.E., Rodbell, D.T., Gillikin, D.P., Aron, P.G., Passey, B.H., Tapia, P.M., Serrepe, A.R., and Abbott, M.B., 2023, Detecting hydrologic distinctions among Andean lakes using clumped and triple oxygen isotopes: Earth and Planetary Science Letters, v. 602, p. 117927, doi:10.1016/j.epsl.2022.117927.

Kelson, J.R., Petersen, S. V., Niemi, N.A., Passey, B.H., and Curley, A.N., 2022, Looking upstream with clumped and triple oxygen isotopes of estuarine oyster shells in the early Eocene of California, USA: Geology, doi:10.1130/G49634.1.

Laskar, J., Robutel, P., Joutel, F., Gastineau, M., Correia, A.C.M., and Levrard, B., 2004, A long-term numerical solution for the insolation quantities of the Earth: Astronomy & Astrophysics, v. 428, p. 261–285, doi:10.1051/0004-6361:20041335.

Passey, B.H., and Ji, H., 2019, On the use of triple oxygen isotopes in lake waters and carbonates for reconstructing $\delta^{18}O$ of unevaporated precipitation: a case study from the Western United States: Earth and Planetary Science Letters, v. 518, p. 1–12, doi:10.1016/j.epsl.2019.04.026.

Reimer, P.J. et al., 2013, IntCal13 and Marine13 Radiocarbon Age Calibration Curves 0–50,000 Years cal BP: Radiocarbon, v. 55, p. 1869–1887, doi:10.2458/azu_js_rc.55.16947.

Seltzer, G., Rodbell, D., and Burns, S., 2000, Isotopic evidence for late Quaternary climatic change in tropical South America: Geology, v. 28, p. 35, doi:10.1130/0091-7613(2000)28<35:IEFLQC>2.0.CO;2.

Surma, J., Assonov, S., Herwartz, D., Voigt, C., and Staubwasser, M., 2018, The evolution of ^{17}O-excess in surface water of the arid environment during recharge and evaporation: Scientific Reports, v. 8, p. 4972, doi:10.1038/s41598-018-23151-6.

Thompson, L.G., Mosely-Thompson, E., Davis, M.E., Lin, P.-N., Henderson, K.A., Cole-Dai, J., Bolzan, J.F., and Liu, K. -b., 1995, Late Glacial Stage and Holocene Tropical Ice Core Records from Huascaran, Peru: Science, v. 269, p. 46–50.

Voigt, C., Herwartz, D., Dorador, C., and Staubwasser, M., 2021, Triple oxygen isotope systematics of evaporation and mixing processes in a dynamic desert lake system: Hydrology and Earth System Sciences, v. 25, p. 1211–1228, doi:10.5194/hess-25-1211-2021.